HHS Public Access

Author manuscript

Med Phys. Author manuscript; available in PMC 2021 October 07.

Published in final edited form as:

Med Phys. 2020 August ; 47(8): 3752–3771. doi:10.1002/mp.14241.

Multi-energy computed tomography and material quantification: Current barriers and opportunities for advancement

Megan C. Jacobsen[a)], **Sara L. Thrower**

Department of Imaging Physics, The University of Texas MD Anderson Cancer Center, Houston, TX 77030, USA

Rachel B. Ger,

Department of Radiation Physics, The University of Texas MD Anderson Cancer Center, Houston, TX 77030, USA

Shuai Leng,

Department of Radiology, Mayo Clinic, Rochester, MN 55905, USA

Laurence E. Court,

Department of Radiation Physics, The University of Texas MD Anderson Cancer Center, Houston, TX 77030, USA

Kristy K. Brock,

Department of Imaging Physics, The University of Texas MD Anderson Cancer Center, Houston, TX 77030, USA

Eric P. Tamm,

Department of Abdominal Imaging, The University of Texas MD Anderson Cancer Center, Houston, TX 77030, USA

Erik N.K. Cressman

Department of Interventional Radiology, The University of Texas MD Anderson Cancer Center, Houston, TX 77030, USA

Dianna D. Cody, **Rick R. Layman**

Department of Imaging Physics, The University of Texas MD Anderson Cancer Center, Houston, TX 77030, USA

Abstract

Computed tomography (CT) technology has rapidly evolved since its introduction in the 1970s. It is a highly important diagnostic tool for clinicians as demonstrated by the significant increase in utilization over several decades. However, much of the effort to develop and advance CT applications has been focused on improving visual sensitivity and reducing radiation dose. In comparison to these areas, improvements in quantitative CT have lagged behind. While this could be a consequence of the technological limitations of conventional CT, advanced dual-energy CT (DECT) and photon-counting detector CT (PCD-CT) offer new opportunities for quantitation. Routine use of DECT is becoming more widely available and PCD-CT is rapidly developing.

[a)]Author to whom correspondence should be addressed. mcjacobsen@mdanderson.org; Telephone: 713-794-4055.

This review covers efforts to address an unmet need for improved quantitative imaging to better characterize disease, identify biomarkers, and evaluate therapeutic response, with an emphasis on multi-energy CT applications. The review will primarily discuss applications that have utilized quantitative metrics using both conventional and DECT, such as bone mineral density measurement, evaluation of renal lesions, and diagnosis of fatty liver disease. Other topics that will be discussed include efforts to improve quantitative CT volumetry and radiomics. Finally, we will address the use of quantitative CT to enhance image-guided techniques for surgery, radiotherapy and interventions and provide unique opportunities for development of new contrast agents.

Keywords

dual-energy computed tomography; photon-counting detector computed tomography; quantitative computed tomography

1. INTRODUCTION

1.A. Organization and scope of the paper

Conventional, dual-energy, and photon-counting detector computed tomography (CT) can each be used to make quantitative measurements that inform and improve clinical decision-making, and each evolution in these technologies has enabled the use of novel image types for this purpose. This paper focuses on the use of quantitative metrics derived from CT for clinical use, with an emphasis on applications of multi-energy CT (MECT). Section 1 gives background information regarding conventional CT, dual-energy CT (DECT), and photon-counting detector CT (PCD-CT). Section 2 details use of DECT for several quantitative applications with an emphasis on the historical use of conventional CT. There is relatively little research performed using dual-energy CT as an input to pharmacokinetic models; rather, DECT has primarily been investigated as a surrogate for perfusion CT due to the lower radiation dose and imaging time. Therefore, perfusion or dynamic contrast-enhanced CT quantitation is beyond the scope of this paper. Comprehensive reviews of perfusion CT are cited here.[1–3] The limitations of quantification with conventional, dual-energy, and PCD-CT are summarized in Section 3, while Section 4 covers emerging developments in the field of quantitative MECT. Discussion of the quantitative MECT's potential to impact clinical practice is presented in Section 5, with conclusions in Section 6.

1.B. Conventional CT

The first clinical CT scanner was introduced in the early 1970s, and quantitative uses for the system were in development by the end of the decade. Computed tomography data consists of x-ray transmission measurements taken at a large number of angles as an x-ray tube rotates around a patient. The x-ray attenuation is a function of the linear attenuation coefficient (μ, measured in units of cm^{-1}) along the x-ray path as well as the thickness of the material it passes through. With data taken from multiple angles, it is possible to use image reconstruction algorithms, such as filtered backprojection, to calculate a map of the linear attenuation coefficients throughout a cross section of the body. However, the linear attenuation coefficient varies based on the energy spectrum, and therefore visualization is aided by normalizing the raw attenuation data to the linear attenuation coefficient of water ($\mu water$). The CT number, measured in Hounsfield Units (HU) was defined as:

$$HU = 1000 \times \frac{\mu_{tissue} - \mu_{water}}{\mu_{water}} \tag{1}$$

where μ represents the linear attenuation coefficient of a given material. The CT number of air, which has virtually no x-ray attenuation, is therefore approximately −1000 HU while the CT number of water is 0 HU regardless of the energy spectrum used for scanning. It became clear that quantitative measurements of CT number could be correlated with disease processes. Early quantitative imaging applications focused primarily on uses of the CT number for tissue and disease characterization,[4–6] bone mineral density measurement,[7–13] and volumetry.[14,15] Standardized CT number thresholds were developed, which allowed for differentiation between materials such as intracranial hemorrhage and calcification[16,17] and to define contrast enhancement in solid renal masses[18–21] with acceptable sensitivity and specificity. As technology has improved, significant advances enabled faster scanning, thinner images, minimization of artifacts, and decreased variability — verified through required quality control programs[22] — in quantitative measurements in patients over time.

1.C. Dual-energy CT

Dual-energy CT was conceived by Godfrey Hounsfield in 1973,[23] and the concept was further investigated by Alvarez and Marcovski[24] in 1976. Dual-energy CT became commercially viable with the release of the first dual-source DECT system in 2006. In DECT, two x-ray spectra are acquired with different peak energies to provide energy dependent information about the photoelectric and Compton scatter components of a voxel's attenuation. This enables advanced applications in which material-specific images[24–26] (e.g., iodine) and synthetic monoenergetic images[27] may be generated. Material-specific images are generated using material decomposition algorithms. These algorithms utilize a linear combination of the photoelectric and Compton effects for two or more chosen materials within a given voxel to estimate the volume fraction of each basis material present. Since material decomposition algorithms typically assume that only the chosen basis materials are present within each voxel, proper identification of the materials relevant to each application is paramount for accurate quantification. Several examples of clinically available applications for specific material decompositions are shown in Table I. Synthesized monoenergetic images are created by summing the attenuation of the estimated amount of iodine and water in a voxel at a specific energy, typically between 40 and 200 keV. By measuring the attenuation at multiple synthesized energy levels, a simulated transmission spectrum can be generated and potentially used to identify tissue types. Monoenergetic images have been used semi-quantitatively for improved image contrast, thus this review will focus primarily on the quantitative use of material-specific images.

1.D. Photon-counting detector CT

Recently, PCD-CT has become technologically feasible for true multi-energy CT scanning, and has been used in multiple preclinical and clinical studies.[28–35] This represents an evolution of the methods for collecting CT data within the energy domain; similarly to

DECT, the data can be processed into material-specific or virtual monoenergetic images. Photon-counting detectors use direct conversion techniques, where incident x rays are absorbed in semiconductor detector material [e.g., cadmium telluride (CdTe), cadmium zinc telluride (CZT), gallium arsenide (GaAs) or silicon], generating a cloud of electron-holes paired with charges proportional to the energy of the incoming photon. Electrons are then attracted to the readout electronics by means of a large bias voltage placed over the semiconductor layer. In an ideal detector, each x ray absorbed by the semiconductor layer would result in an individual electrical pulse, and the height of the pulse would indicate the x-ray energy. By setting different energy thresholds, incoming photons can be placed in discrete bins, and small pulses caused by electronic noise can be removed from the data. Because the data can theoretically be split into multiple energy bins with minimal overlap, there is potential for PCD-CT to provide opportunities for improved quantification with material decomposition relative to DECT. However, existing PCDs do not operate as ideal detectors since significant spectral overlap remains a concern (see Section 3.C for additional details). Photon-counting detectors do provide temporally and spatially co-registered projections for all energy windows, which can minimize artifacts relative to DECT.[36] Furthermore, PCD-CT can allow for imaging a wider variety of potential contrast agents,[35,37] minimized electronic noise relative to DECT acquisitions,[38] and concurrent use of multi-energy and high spatial resolution modes[36] that is not available on all DECT systems.

A major advantage of PCD-CT over DECT is the potential improvement in material decomposition, particularly for materials with K-edges within the diagnostic energy range. While the differing physical spectra provide some unique material information in DECT, PCD-CT allows users to select specific energy bins to provide improved spectral separation, which may result in better accuracy for material differentiation compared to DECT. Additionally, the number of energy bins and their energy ranges can be chosen to further optimize multi-material decomposition. For example, four-material decomposition is possible in cases where multiple materials with K-edges in the diagnostic range are present[39] (see Section 4.A for a discussion of novel contrast agents). This avoids the use of *a priori* constraints such as volume conservation that are commonly used in DECT material decomposition algorithms. Application of more energy bins with PCD-CT material decomposition could improve material differentiation for disease characterization, evaluation for response to therapy or enable simultaneous administration of multiple contrast agents. In phantom studies, PCD-CT has been shown to accurately measure material concentrations of iodine, gadolinium, and calcium.[40,41]

2. CURRENT APPLICATIONS OF QUANTITATIVE CT

2.A. Tumor volumetry

Recent efforts spearheaded by the Radiological Society of North America's quantitative imaging biomarkers alliance (QIBA) have approved a profile for measurement of tumor volume change[42] and have reached a consensus regarding CT volume assessment of small lung nodules.[43] For measurement of tumor changes in metastatic disease, the longitudinal monitoring of treatment response and disease progression in solid tumors is critical.

Quantitative measurements of tumor volume change have gone through multiple standards since the publication of the first World Health Organization guidelines in 1981,[44] including response evaluation criteria in solid tumors (RECIST), where the longest diameter of multiple lesions are measured and followed over time.[45] In the most recent update, RECIST 1.1, response to treatment is determined by summing the measured diameters of up to five representative lesions or metastatic lymph nodes that measure at least 10 mm in diameter at baseline and comparing the sum over time.[46]

There are several documented issues with these measurements. RECIST criteria related to diameter measurements has several limitations that may be resolved by using tumor volumetry as a metric, including the variability in tumor shape and the lack of measurements in orthogonal planes. Nevertheless, RECIST 1.1 has been utilized as a primary endpoint in Phase III drug trials and is considered to provide strong evidence for complete or partial response. QIBA has provided guidance about the confidence clinicians can expect under standard acquisition conditions. Overall, they assert that a 95% confidence interval of 30% for change in tumor volume from baseline is achievable based on a conservative estimate of variation in quantitative values due to slight differences in protocol, patient positioning, contrast administration, and measurement variability.[42] Therefore, a change of at least 30% or more volume should be suggestive of significant change from baseline, and may be indicative of either response to treatment or progressive disease.

One primary weakness of using CT volumetry and RECIST criteria is the response of certain hypervascular tumors on CT imaging. Specifically, the response of tumors such as Gastrointestinal Stromal Tumors (GIST) and certain renal cell carcinomas (RCC) to certain biologic drugs, including imatinib (Gleevec®, Novartis, Basel, Switzerland) and other molecularly-targeted antiangiogenic agents, do not demonstrate volume changes but rather variation in tumor perfusion metrics such as reduced vascularity. In 2007, Choi et al. published a study that indicated that the size of imatinib-treated GIST was not the primary marker of response to treatment; rather, attenuation differences on contrast-enhanced CT correlated strongly with a decrease in standardized uptake value on PET/CT for marked response to treatment.[47,48] The initial Choi criteria for partial response was defined as a decrease in the largest unidimensional diameter of a lesion of >10% or more than a 15% decrease in CT number.[47,48] Similarly, progressive disease was determined by a tumor diameter increasing by more than 10%.[47,48] An update to this rule, known as Modified Choi Criteria, requires both a decrease in diameter and a drop in attenuation to qualify as a partial response.[49] Therefore, it is critical to appreciate disease heterogeneity, with respect to type of solid tumor involved as well as the therapeutic treatment provided, in order to appropriately apply volumetric CT metrics.

2.B. Bone mineral density

The prevalence of osteoporosis, clinically significant bone mineral density loss, amongst the population of the United States in women above 50 yr of age is estimated to be approximately 29.9% according to a recent study by Wright et al.[50] For those 80 yr of age or older, the prevalence of significant bone loss increased to 46.3% in men and 77.1% in women.[50] Fragility fractures related to osteoporosis frequently occur in the hip, vertebrae, wrist, and humerus, resulting in severe morbidity and increased financial burden, particularly among elderly populations.[51,52]

Dual-energy x-ray absorptiometry (DEXA) is the primary method for measurement of BMD in use clinically; however, DEXA measurements of areal bone density are affected by patient height,[53] weight,[54–56] and distribution of adipose tissue.[57–59] Additionally, there is a risk of misinterpreting DEXA-based BMD measurements in pediatric subjects.[60] Dual-energy x-ray absorptiometry measurements are also demonstrated to be unreliable in patients with degenerative changes in the bone.[61,62] The tomographic reconstructions in CT have been shown to improve quantitation in many subjects in which DEXA fails,[7] although QIBA has not yet developed a profile on this topic. Quantitative CT BMD measurements are primarily made in reference to calibration phantoms, which provide known quantities of bone-equivalent materials such as potassium phosphate[63] (QCT PRO; Mindways Software, Inc.; Austin, TX) or a combination of water-equivalent and hydroxyapatite-doped plastics.[64] These calibration phantoms can either be placed underneath patients (example in Fig. 1) as they are scanned on clinical CT systems to provide an external reference for determining the HU expected for various concentrations of bone[63,64] or a quality control phantom can be scanned at another time to measure BMD using an asynchronous technique.[65] Examples of phantom-less techniques include using muscle and fat to calibrate the HU of bone[66,67] or using the CT number of trabecular bone directly.[68,69] Using internal calibrations results in errors of up to 1.1% in vertebrae relative to phantom-calibrated scans, while using uncalibrated CT numbers alone is sensitive to variations in tube voltage and body habitus.[70]

While DEXA provides a T-score — the number of standard deviations from the average BMD of a healthy 30-yr-old — to determine whether BMD indicates the presence of osteopenia or osteoporosis, spinal CT BMD measurements cannot be directly compared to DEXA-derived areal BMD. However, CT of the proximal femur can be reconstructed to simulate a projection radiograph in the orientation of a DEXA acquisition from which areal BMD can be compared directly in the pelvis,[71] and the two modalities have been shown to correlate very well.[72] CT-derived BMD of the proximal femur scanned concurrently with a calibration phantom could explain up to 76% of variance in femoral bone strength compared to 69% for DEXA.[73] The American College of Radiology (ACR) practice guidelines recommend using the diagnostic criteria in Table II to avoid overestimating the fracture risk of patients from spinal CT[74] as well as following individual patients on the same CT unit if possible.[74] It is expected that age related bone density loss in postmenopausal women is between 0.7 and 1.9% per year in white populations,[75,76] but DEXA measurements do not differentiate between losses in cortical versus trabecular bone. Overall, recent studies of quantitative BMD measurements with CT have shown that the coefficient of variation is low when CT operators are well trained, ranging from 0.6 to 3.3%[66,77]; in comparison, the coefficient of variation for DEXA measurements is between 0.5 and 2.5%.[77]

Measurements of BMD with DECT may be more accurate than those measured by DEXA and conventional CT, particularly in instances where phantom calibration is asynchronous. The initial DECT BMD studies were published in the 1980s,[78–80] but have recently gained popularity as DECT examinations have become more common clinically. In a conventional CT image of trabecular bone, many voxels contain a mixture of bone marrow (primarily adipose) and trabeculae, which ultimately leads to inaccurate CT numbers that may artificially lead to trabecular bone volume uncertainties of up to 15%.[7,81] In comparison, DECT with three-basis material decomposition comprised of calcium (or hydroxyapatite), adipose tissue, and soft tissue has been shown to minimize the dependence of BMD assessment on the fat percentage of the marrow (R^2 = 0.05 for DECT vs. R^2 = 0.56 for SECT, where lower correlation is desirable),[82] and improve the accuracy and precision of phantom-less imaging techniques.[83] Wesarg et al.[84] demonstrated that DECT-based BMD also shows better correlation with mechanical force measurements relative to DEXA, with R^2 of 0.82 and 0.48, respectively. While DECT material decomposition is a very promising method for calculating BMD, more work is required to determine the coefficient of variation in a human population. Additionally, hydroxyapatite or calcium concentration measurements from material decomposition algorithms may vary between vendors,[85,86] thus requiring cross-calibration between different DECT platforms.

2.B. Hepatic steatosis (fatty liver disease)

Hepatic steatosis, also known as fatty liver, is the primary symptom of nonalcoholic fatty liver disease (NAFLD), which has an estimated prevalence of approximately 25% worldwide.[87] common etiologies include, but are not limited to, alcohol consumption,[88] hepatitis C,[89,90] and use of certain medications[91] — including many chemotherapies[92,93] and corticosteroids.[94] Nonalcoholic fatty liver disease is also associated with metabolic syndrome, a set of risk factors for cardiovascular disease and type II diabetes that include obesity, hypertension, elevated triglycerides, and insulin resistance.[95,96] Nonalcoholic fatty liver disease is a risk factor for liver cirrhosis[97,98] and hepatocellular carcinoma (HCC).[99,100] In addition to the disease burden caused by NAFLD, hepatic steatosis is also associated with poor outcomes for surgical interventions in the liver.[101–103] The current gold standard for the quantification of liver fat with imaging is magnetic resonance imaging (MRI) Dixon-based sequences, which allow for measurement of the proton density fat fraction (PDFF).[104–107] This has largely replaced MR spectroscopy,[108–110] which is time consuming and typically is performed using a single large voxel that makes it prone to both volume averaging and sampling error. To date, QIBA has not yet published a profile on quantification of hepatic steatosis with CT.

With conventional CT, fatty liver is best diagnosed on non-contrast examinations[111] because contrast-enhanced CT has limited sensitivity caused by variability in contrast administration, timing, and variations in perfusion. Kodama et al. demonstrated this by showing pathologic fat content had a higher correlation with unenhanced CT HU (R^2 = 0.649) than contrast-enhanced CT HU (R^2 = 0.516).[112] Other groups have converted CT HU measurements directly to fat fraction using in-scan calibration phantoms, and found that calculated adipose content using the calibration curves were correlated with liver fat upon biopsy (R^2 = 0.689).[113] In phantoms, Pickhardt et al. also found that CT HU at 120 kVp measurements were highly correlated with MRI-PDFF (R^2 = 0.828), but single-energy CT tended to underestimate the liver fat content when iron overload was present[114] since higher iron content increases the background attenuation in the tissue. Overall, fatty liver is typically diagnosed with CT when the liver attenuation is either below 40 or 10 HU less than the attenuation of the spleen[115–117] (Fig. 2), which does not aim to quantify the fat percentage, but rather indicates the presence or absence of hepatic steatosis.

Dual-energy CT with three-material decomposition may also provide additional accuracy for fat segmentation and quantification tasks since it is possible to estimate the fat fraction within the tissue directly (Fig. 3). Several studies have shown that unenhanced DECT using a water-fat material decomposition algorithm alone does not significantly increase the correlation of CT fat fraction and MR-PDFF fat fraction versus single-energy CT.[118–120] However, in a 2016 study by Hyodo et al., a three-material decomposition model based on fat, liver tissue, and contrast agent (iodine) was used in phantoms to accurately assess fat content. They found that while SECT fat estimates demonstrated a dependence on the size of the phantom, DECT fat quantification was largely unaffected by a moderate change in phantom size.[121] The same group assessed the algorithm in patients and found a statistically significant proportional bias in the fat fractions measured on DECT vs. MRS,[122] which may have been a result of either underestimation of fat volume fraction by DECT, overestimation of fat content by MRS, or variations in iron levels that were associated with the steatosis. These algorithms are also useful for differentiating between lipid-poor and lipid-rich abdominal lesions in the adrenal glands.[123,124] Dual-source DECT has been shown to separate hepatic iron and fat in phantoms[125,126] with a fat, soft tissue, and iron decomposition; however, this algorithm did not provide a percent fat fraction, so a calibration between a virtual non-iron pseudo-HU and pathological fat would be required to directly measure the amount of fat present.[127] Overall, DECT has shown to have significant advantages over conventional CT for the estimation of fat content in the presence of either iodinated contrast or iron overload in liver tissue.

2.C. Renal Cell Carcinoma

Renal cell carcinomas (RCCs) represent 80–85% of primary neoplasms in the kidney, and it is estimated that 65 340 people in the United States were newly diagnosed with renal malignancies in 2018, with an additional 14 970 dying of the disease.[128] There are several imaging criteria that may indicate that a renal lesion is malignant, including the absence of a significant fatty component, contrast enhancement of 15–20 HU,[18,129] cystic components with enhancement (Bosniak types III and IV),[19,20] and tumor complexity. There are a variety of RCC subtypes that represent different tumor morphology, cellular origin, and growth patterns. These subtypes, with their relative incidences, include clear cell (75–85%), papillary or chromophilic (10–15%), chromophobe (5–10%), and oncocytic (3–7%).[130,131] Additionally, fat-poor angiomyolipomas and oncocytomas complicate the differential diagnosis of RCC with imaging alone. While CT imaging is common for renal disease, QIBA has not yet published a profile regarding quantitative analysis of CT number or iodine concentration for differentiation of these lesion types.

Evaluation of mean CT number alone has been shown to lack specificity for differentiating fat-poor angiomyolipoma and oncocytoma from various subtypes of RCC.[132,133] In order to differentiate between these etiologies with conventional CT, quantitative techniques such as texture analysis are currently being investigated. Sasaguri et al. found that CT attenuation and histogram skewness on both the corticomedullary and nephrographic phases were able to differentiate oncocytoma from clear cell RCC (AUC = 0.82) and papillary RCC (AUC = 0.95)[134] in small lesions; while they found that subjective lesion inhomogeneity was significant, entropy, a texture feature used to quantify pixel randomness, did not reach the level of significance in a multi-variate analysis. Hodgdon et al. evaluated patients with fat-poor angiomyolipoma and RCC and found that models based on various combinations of three unenhanced CT texture features could achieve an AUC between 0.85 and 0.89, with quantitative measures of homogeneity and entropy having the highest predictive power for diagnosis of RCC.[135] These studies have begun to suggest that quantitative measures of inhomogeneity may be more sensitive than subjective metrics assigned by a radiologist.

DECT has been shown to be particularly valuable for renal imaging, with applications for differentiating subtypes of RCC from cysts[136–138] as well as classifying renal stone composition.[139] Renal lesions under 4 cm in diameter are a frequent incidental finding on clinical imaging.[134,140] Multiple quantitative metrics, including measured iodine concentration,[137,141–143] monoenergetic attenuation,[144–146] and effective atomic number (Z_{eff})[147] have improved the differentiation of benign and malignant renal lesions. One study by Manoharan et al. is particularly notable because it demonstrated non-inferiority of DECT iodine quantification compared to conventional CT for the evaluation of renal masses in a prospective, randomized controlled trial despite a lower radiation dose with the DECT exams.[141] Several studies have demonstrated that iodine quantification was able to distinguish between subtypes of renal cell carcinoma, including clear cell and low-enhancing papillary variants, as well as fat-poor angiomyolipomas.[148–151] Both Chandarana et al. and Mileto et al. demonstrated that 0.5 mg/mL iodine in a renal lesion was sufficient to distinguish non-enhancing from enhancing renal lesions using dual-source DECT[137,138]; furthermore, the second group also found an optimal threshold of 0.9 mg/mL for differentiating papillary and clear cell RCCs.[148] Counter to this, Kaza et al. found that the optimal threshold between enhancing and non-enhancing RCCs was 2.0 mg/mL on a fast kVp switching DECT system.[136] Some of this difference may be attributed to differences in contrast timing between the scan protocols on the two DECT systems; as a result, there is an opportunity for protocol standardization to minimize variance across DECT implementations by different manufacturers.

2.D. Radiotherapy treatment planning

CT numbers have been used extensively since the introduction of the modality to quantify the attenuation of nonuniform tissue for dose calculations in radiotherapy.[152,153] CT numbers are used to estimate the electron density of tissue for photon radiotherapy[154] or proton stopping power for proton therapy.[155] Historically, tissue substitutes were used to calibrate the CT number to specific electron density[154,156] using a bilinear fit, but this technique was dependent on the location of the material of interest within the patient, the accuracy of the CT number itself, and the scanner model.[157] Schneider et al. developed the stoichiometric calibration to more accurately determine the electron density of biological tissues, which improved the mean error in calculated electron density from 2.5% with the tissue substitute method to 0.5% and minimized the number of pixels with more than a 2% deviation from the true electron density.[157] Nakao et al. found that the typical dose errors resulting from day-to-day differences in CT constancy were typically within a range of −0.9

to 0.1% for 6 MV lung plans, and between −1.0 and −1.6% for 10 MV prostate plans[158]; this demonstrates the dependence of the electron density conversion on depth originally found by Kilby et al.[159] However, there remains some subjectivity in the application of the stoichiometric method due to the number of line segments the users choose to fit to the calibration data.[160,161] Furthermore, while convolution- or superposition-based treatment planning algorithms only require tissue electron density as an input, Monte Carlo-based treatment planning requires additional material information such as the elemental mass percentages[162–165] to be calculated from the CT data.

Dual-energy CT provides the ability to calculate Z_{eff} and electron density (q_e), which is advantageous for radiotherapy treatment planning. In particular, the accuracy of the CT-calculated proton stopping power ratio has a direct impact on the proton range estimate, which is critical because there is a sharp dose gradient at the Bragg peak.[166] In addition to the dose gradient, there is also a demonstrated change in the proton LET along the proton range,[167,168] which directly impacts the deposited dose. The stoichiometric method has recently been adapted for DECT data, and it has been shown to improve the accuracy of proton stopping power calculations in validation studies.[169–173] Zhu et al. found that error in stopping power calculated with SECT in a phantom of known composition was as high as 12.8% while DECT resulted in only a 2.2% error, which resulted in dose errors of 7.8% and 1.4% for the SECT and DECT plans, respectively.[166] Dual-energy CT metrics have been evaluated using ground-truth maps by Wohlfahrt et al., who found that several DECT-based stopping power predictions could reliably predict stopping power ratio to within 1% deviation from the median[174] using both electron density/effective atomic number[175] and electron density/photon absorption cross section[176] decompositions. However, they were not able to definitively show that this improved the proton range estimate relative to SECT because the smoothing performed on the SECT and DECT differed relative to the ground-truth map.[174] It is generally agreed that the DECT proton range estimation is lower than that of SECT-based calculations,[170,174,177] but clinical significance has yet to be determined. More recent studies have suggested that DECT may be more accurate and result in lower proton range errors when the beam is in the presence of bone.[178]

As discussed previously, it is difficult to accurately determine material characteristics using conventional CT for Monte Carlo treatment planning, both for photon and proton radiotherapy. Several studies have used DECT to estimate material compositions for radiotherapy purposes, including estimations of the water-equivalent path length of protons[179] and tissue oxygen and carbon percentages[180] in addition to calculation of Z_{eff}.[181] An early study by Bazalova et al. reported that Z_{eff} and electron density estimates from DECT were 3.7% and 3.1%, respectively, when simulating DECT acquisitions at 100/140 kVp with 9 mm of additional aluminum filtration.[182] Using a clinically available second generation dual-source system, Landry et al. found that DECT Z_{eff} quantification accuracy was within ±10% across a range of tissue substitutes, while electron density accuracy was within 2.5%.[181] For low-energy brachytherapy applications, additional optimization of the DECT reconstructions, including the use of iterative reconstruction algorithms can further reduce the standard deviation in Z_{eff} and electron density and results in maximum dose calculation errors of 6% compared to 21% for SECT.[183] Dual-energy CT also has been shown to reduce metal artifacts in the presence of implants[184] and metallic brachytherapy seeds,[185] which allows for improved tissue identification[186] and electron density estimation[187,188] for treatment planning.

2.E. Radiomics

Radiomics involves evaluating images at the voxel level to extract quantitative image features (i.e., texture). These radiomics features are then used to build predictive models for overall survival, loco-regional control, or to classify tumors into groupings that may direct treatment. One example of this is using radiomics data from segmented non-small cell lung cancer tumors to stratify patients into varying outcome brackets[189]; in this study, an example of a textural feature that was prognostic of survival was tumor compactness, a measure of how spiculated or smooth the tumor may appear. Other models may utilize texture features to differentiate between benign and malignant tumors.

The radiomics features used in most studies are those that come from intensity histograms (e.g., variance, kurtosis, skewness), gray level co-occurrence matrices, defined by Haralick,[190] gray level run length matrices defined by Galloway and Tang in 1975 and 1998, respectively,[191,192] and neighborhood gray tone difference matrices defined by Amadasun and King.[193] Some additional categories that branch off of these original feature categories have been developed in the past ten years, such as gray level size zone matrix.[194] Recently, the term radiomics has also been used for deep learning approaches that have the same end goal, such as predicting overall survival in cancer patients.

The typical radiomics workflow is comprised of imaging, segmentation, feature extraction, and statistical analysis or cross-validation (Fig. 4). Within this process, there are many confounding factors that could add noise to data sets. Many specific imaging protocol parameters have been investigated to determine their impact on radiomics feature variability, including image thickness, the use of iterative reconstruction versus filtered backprojection, and tube current.[195,196] A recent study combined much of this information and devised a harmonized protocol across different manufacturers and demonstrated that protocol standardization could reduce interscanner variation by over 50% compared to the use of local protocols.[197] However, application of this harmonized protocol has not yet been used for analysis of patient studies. The next radiomics workflow step involves segmentation of the tissue or lesion of interest. This can be performed using CT simulation scans of radiotherapy patients with contours performed by the treating radiation oncologist or application of commercially available tools.[198] Feature extraction from the segmented regions can then be performed using a variety of different software packages, including commercial, open-source, and in-house software.[198] Preprocessing, such as smoothing, is sometimes applied to images before feature extraction. The Image Biomarker Standardization Initiative has attempted to help align features from different software by providing clear definitions and test data sets to benchmark extracted feature values.[199] However, there are still differences in features extracted from different software packages.[200] The final step, statistical analysis, can also have potential pitfalls. One study showed that the statistical methodology of some early studies in radiomics could produce spurious correlations.[201] In each radiomics step, there are areas that still need to be standardized, and these efforts are currently underway.[202] Radiomics has shown promise, in particular in stratifying cancer patients into high or low risk for survival.[203] Incorporating these standardization efforts into more studies will help make studies applicable to the larger community and draw radiomics one step closer to clinical applicability.

2.F. Potential applications of photon-counting CT

There are several promising clinical applications of quantitative PCD-CT. Because the existing PCD-CT systems are in the preclinical stage, most studies have been performed in phantoms, animals, *ex vivo* tissue, or cadavers. However, preliminary studies show that PCD-CT is particularly promising for quantitative imaging due to potential improvements in material characterization and increased spatial resolution.

Fat and lean tissue quantification has been evaluated in *ex vivo* tissue phantoms,[205] and phantom and animal studies have shown that calcium concentration can be accurately measured. Accurate calcium quantification combined with assessment of soft tissue composition could be highly relevant to BMD, atherosclerotic plaque[206], and hepatic steatosis evaluations. Several studies have shown that hydroxyapatite and calcium oxalate stones can be differentiated with PCD-CT if the energy bins are chosen correctly.[207–209] These studies demonstrate the capabilities of PCD-CT material differentiation, which can be further exploited with development of novel, targeted contrast agents (See *Novel Contrast Agent Development*).

A special capability of PCD-CT is simultaneous acquisition of high-resolution and multi-energy images, which can't be achieved at the same time with current commercial CT systems using energy integrating detectors. In quantitative tasks that do not require material decomposition, such as lung density and tumor volumetry, PCD-CT has the ability to provide improvements in spatial resolution that could decrease volume averaging at the boundaries of lesions and improve density measurements.[34,210–214] Additionally, for quantitative tasks that were not feasible with conventional CT due to artifact or high noise levels, PCD-CT allows users to limit the effects of electronic noise, beam hardening artifacts, and metal artifacts through selection of energy thresholds for reconstruction.[31,38,213,215–218]

3. LIMITATIONS TO CT QUANTITATION

3.A. Conventional CT

There are several limitations to the quantitative use of conventional CT. While the in-plane spatial resolution is high, material differentiation is challenging due to acquisition techniques using a single polychromatic beam. As a result, tissues may present with similar attenuation levels despite having different elemental compositions. For example, a calcified lesion may be indistinguishable from a lesion enhanced with iodinated contrast. This limits the ability of conventional CT to quantify BMD due to the presence of fat in the bone marrow that may lower the overall attenuation, and can limit image contrast when identifying lesion boundaries for volumetric measurements. Other confounding factors such as variation in scanner model[219] and geometry, scan protocol, patient positioning[220] and size,[221,222] and analysis methods may induce significant bias into measurements, and must be controlled over the course of patient treatment. This is obviously not possible in all cases, so it is beneficial for multicenter trials and meta-analyses to calculate the estimated inter- and intra-patient variability.

In particular, patient positioning contributes to image quality issues which may impede diagnosis as well as quantification with conventional CT. When patients are positioned at the wrong table height, the lack of appropriate energy and flux modulation at the bowtie filter may induce beam hardening artifacts and cause increased image noise. Since spatial resolution degrades away from isocenter, mispositioning may also result in poor visualization of fine structures such as small blood vessels or bony detail.[223] Poor patient positioning can also lead to issues with tube current modulation due to magnification factors during the localizer scan, causing the dose to either increase or decrease depending on the direction of the positioning error.[224] In an anthropomorphic phantom, Szczykutowicz et al found up to a 15 HU drop in CT number compared to proper positioning in the posterior mid thorax region when the patient was positioned 4 cm above isocenter; absolute errors increased to 20 HU or greater when the phantom was positioned more than 6 cm above isocenter.[220] Relative noise also increases when patients are imaged away from isocenter.[220,225] Large patient size also exacerbates these issues since there is already a larger risk of beam hardening artifact and truncation artifacts in this patient population as well as higher noise. Hardware solutions such as 3D cameras to assist the technologist in positioning the patient are now commercially available, and initial studies demonstrate that their use significantly lowers the deviation between patient isocenter and scan center.[226,227]

3.B. Dual-energy CT

There are several existing limitations to quantification tasks with DECT. First, while all vendors provide two-material decomposition, three-material decomposition is only offered by a subset of vendors and for limited material combinations. For example, one vendor offers users choices of materials for two-material decomposition, with reconstructions limited to pairs of water, iodine, calcium, and hydroxyapatite (or cortical bone). In comparison, another vendor offers both two- and three-material decomposition, but the materials are set on an application basis (i.e., liver virtual non-contrast materials are soft tissue, fat, and iodine while a conventional virtual non-contrast is based on a decomposition of soft tissue and iodine). These applications have been useful in both test phantoms and clinical scenarios, but have not yet been established as quantitative biomarkers by the metrology standards set forth by QIBA. Additionally, the problem of material decomposition with three or more basis materials is ill-posed because only two energy spectra are used as inputs to the algorithm. To avoid this problem, volume conservation of materials within a voxel is typically assumed, but this assumption may not hold for materials in solution, requiring other constraints such as mass conservation.[228]

Substantial work has been done to improve material decomposition algorithms for DECT over recent years. Liu et al first described the use of mass conservation in three-material decomposition, and the accuracy depended strongly on the difference in the dual-energy ratios of the materials being separated.[228] Several studies have evaluated the use of more than two basis materials in material decomposition, which have the advantage of modeling complex biology or multiple contrast agents within the same object.[120,229,230] Since the accuracy of the CT number impacts material decomposition accuracy as well,[231] algorithms have been developed to correct beam hardening for the purposes of DECT reconstruction.[232] Other groups have focused on improving the noise characteristics of material decomposition images with iterative reconstruction[229,233] and machine learning.[234]

While DECT has enabled many advances in quantitative CT, there are barriers that remain. The spectral separation is inherently limited in several DECT implementations, including dual-layer detector and split-filter systems. Because these systems both use a single polychromatic beam, the average energies of the two spectra used to compute the material decomposition are relatively similar compared to what is possible on a rapid kVp-switching or dual-source system. The spectral overlap increases the image noise and increases variability between measurements, raising the limit of detection for materials, particularly in large patients. For all DECT systems, the lowest kVp spectrum available is generally limited to 70 or 80 kVp because photon starvation becomes an issue in even average-size adults at energies below this threshold. In brain imaging with DECT, beam hardening in the skull base and temporal lobe can alter the CT numbers before they are entered into the material decomposition algorithm. Furthermore, the assumptions made in the DECT material decomposition process do not enable quantitation of materials that have K-edges within the diagnostic energy range, which limits the clinical utility of many novel contrast agents.

3.C. Photon-counting CT

While PCD-CT is a very promising technology, there are many technical limitations that must be addressed before it can be made readily available in a clinical setting. The first is that developing PCD that can handle the high count rates required for fast CT acquisitions is challenging. Pulse pileup occurs when multiple x rays are incident on a detector element within a very small time window and registered as a single, high-energy photon. As count rates increase, this phenomenon is more likely and skews the detected spectrum. Additionally, count-rate drift due to crystal defects can alter the signal output from individual detector elements, which may lead to ring artifacts.[235] Other nonideal detector response issues can alter the detected spectrum as well, including stochastic generation of electron/hole pairs, incomplete charge collection, charge-sharing, cross-talk between two detector elements caused by x-ray incident near the border of two adjacent detector elements, and fluorescent photons (K-escape) released in an element that are absorbed in adjacent detectors and cause charge cascades.[28,236–238] Each of these examples causes a single photon to be read as two or more separate events in different locations, which blurs the image spatially and lowers the energy resolution of the detector. Thus, the expected detector response becomes distorted and results in imperfect spectral separation between the bins.[28,239] Without correction, the estimated attenuation coefficient of water is underestimated, which causes cupping artifacts[239] in addition to causing biases in the material decomposition algorithms.[240] A wide variety of solutions have been proposed for these issues, including detector hardware,[241,242] improved bowtie filters to optimize photon flux,[243,244] and image reconstruction algorithms.[238,245,246]

4. FUTURE APPLICATIONS FOR QUANTITATIVE CT

4.A. Novel contrast agent development

Nonionic iodinated agents are the primary form of exogenous contrast used in CT imaging, but there is a small risk of allergic-like reactions ranging from mild (uricaria, nausea, pruritus) to severe (anaphylactic shock) in patients with certain risk factors such as asthma.[247–249] The rate of acute allergic-type reactions to nonionic, low-osmolality iodinated contrast has been estimated at 0.2–0.7%.[250–252] Barium sulfate is also administered orally for certain exams to provide positive contrast in the gastrointestinal tract,[253,254] and xenon-enhanced CT has been used to assess lung ventilation[255] and cerebral blood flow.[256,257] The advent of DECT, and particularly PCD-CT, has resulted in increased interest in the use and development of contrast agents using materials that have dual-energy ratios (the HU ratio between low and high kVp) and/or K-edges that differ from iodine. Lambert et al. showed that certain high-Z materials can be differentiated using DECT based on their dual-energy ratios.[258] This algorithm was validated in phantoms of coronary arteries with simulated calcific plaques, which were filled with either tungsten or iodine contrast; overall, the error in calcium scores with tungsten contrast agent were 16.3% and 6.4% for DECT material decomposition and their methodology. Respectively, the errors were 39.8% and 9.7% when using iodinated contrast with material decomposition and this method.[259]

There are several high-Z materials that have K-edges between approximately 40 and 100 keV that are of interest for K-edge imaging with PCD-CT. This technique uses material decomposition with energy bins specifically placed below and above the K-edge of a material for more accurate quantification, as demonstrated in Fig. 5. This can be achieved using filtration on conventional CT systems, as originally conceived by Riederer and Mistretta,[261] or through optimal choice of energy bins in PCD-CT. Figure 6 shows how the attenuation of gadolinium in phantoms dramatically increases with an energy bin placed just above the K-edge of 50.2 keV. While this is useful from an imaging standpoint, the main drawback of the use of gadolinium as a CT contrast agent is that the concentrations required may leave patients at a higher risk for nephrogenic systemic fibrosis; additionally, several studies have demonstrated gadolinium deposition in deep gray matter of the brain following multiple MRI studies.[262,263] Therefore, significant effort is ongoing for contrast agents based on gold, tungsten, ytterbium, and tantalum (K-edges shown in Table III).[264]

Gold nanoparticles have been utilized extensively for a wide range of imaging applications, including both CT and MRI. While it does increase vascular contrast on conventional CT,[264] other novel contrast agents provide more contrast in the vasculature and organs at substantially lower cost. However, tumor-specific imaging with targeted[266–268] or theranostic agents[269] could be indications that justify the cost.

Tungsten has been used in a dual-contrast dual-energy imaging scheme with iodinated contrast in bowel imaging, and is more promising for this application than bismuth.[270,271] Tungsten has also been demonstrated as a theranostic agent,[272,273] acting as a contrast agent for PCD-CT and an agent to enhance photothermal therapy. However, a potential disadvantage of using tungsten-based contrast agents in CT is that there is low x-ray fluence just above the two K-edges due to self-filtration in the tungsten anode that could potentially reduce image contrast relative to other nanoparticle formulations.

Ytterbium was proposed as a CT contrast agent by Unger and Gutierrez in 1986, and it was found to be visually more dense than iodine at comparable concentrations.[274] More recent studies have utilized ytterbium nanoparticles, which are particularly useful for vascular imaging due to their longer circulation time in the blood pool when pegylated.[275,276] Pan et al. have also developed a stable Ytterbium lipid-encapsulated nanocolloid[277] that could accurately identify non-targeted ytterbium within a mouse heart with PCD-CT. The long-term goal is to develop a compound targeted to fibrin, which may be advantageous for detecting unstable atherosclerotic plaques *in vivo*.[277] Despite these potential advantages, the amount of ytterbium currently being produced worldwide would not be sufficient for frequent medical use in a large population.[264]

Tantalum has similar attenuation properties to ytterbium on conventional CT and has been investigated as a CT contrast agent in multiple forms. Like ytterbium, tantalum-based nanoparticles may be useful for vascular imaging, and several studies have demonstrated biocompatability[278,279] and have been validated in porcine models[280] with various tantalum oxide (TaCZ) nanoparticle formulations. Other researchers have focused on the possibility of using tantalum oxide cores with various nanoparticle shells to create multi-modality imaging agents compatible with CT, MRI, and either photoacoustic or luminescence[281] imaging. Tantalum can also be conjugated with doxorubicin as a theranostic agent, which may enable the quantitative tracking of cancer therapies, the feasibility of which has been shown with DECT imaging of platinum-based chemotherapeutic agents. Additional studies have demonstrated a tantalum shell as a simultaneous dual-modality imaging agent, a vessel for chemotherapeutic agents, and a heat sensitizer to treat esophageal malignancies.[282,283] In combination with PCD-CT, tantalum oxide has tremendous potential to quantify drug delivery and improve the delivery of thermal therapies as well as acting as a vascular agent in conventional CT.

4.B. Radiotherapy applications

DECT acquisitions of contrast-enhanced CT simulation exams could provide both contrast-enhanced CT images for optimal physician contouring along with virtual non-contrast CT for dose calculation as a replacement for a true non-contrast scan. However, dose calculations based on virtual non-contrast-enhanced scans still needs to be validated on a large patient cohort with a direct comparison to conventional non-contrast CT. Furthermore, advanced synthesized monoenergetic reconstructions of dual-energy scans have the ability to provide low noise and reduced artifacts and improved image contrast relative to conventional CT by combining the low-frequency data from the low-energy image set and the high-frequency data from the high-energy image set.[284] Monoenergetic images have been shown to improve image quality over a blended CT image equivalent to 120 kVp.[285,286] Both Kaup[286] and Wichmann[285] tested 40, 60, 80, and 100 keV synthesized monoenergetic images for viewing lesions in the lung and head and neck, respectively. Both studies concluded that lesion contrast was greatest at 40 keV, but the contrast-to-noise ratio was optimized at 60 keV. Optimal scan parameters for image quality and dose calculations vary across studies, and further work is needed to determine best practices. Additional studies are required to objectively quantify the effect this improved image quality has on physician contours of tumor and normal tissue structures across a large patient population.

Studies have shown the benefit of DECT[174,287] and photon-counting CT[288] for improved calculation of stopping power ratio in proton therapy planning. However, the clinical implementation of DECT for proton therapy is widely varied across institutions, making its true clinical impact difficult to discern.[289] Future work is needed to optimize and standardize the use of DECT for stopping power ratio calculations in proton therapy applications. A step-wise approach to the implementation of DECT for proton therapy planning has been proposed, which would begin with transitioning from conventional CT to virtual monoenergetic images from DECT, and finally to DECT-based electron density estimates,[290] to enable adoption by clinics, commercial treatment planning software, and regulatory bodies.

The ability of DECT to quantify the presence of high-Z materials will make it an important tool for future nanoparticle-enhanced radiation therapy. The radiation dose-enhancing effects of gold nanoparticles has been thoroughly investigated in simulations, *in vitro* and *in vivo* small animal studies.[291] Dual-energy CT and PCD-CT have shown the ability to quantify the distribution of gold nanoparticles in simulations, *in vitro* and *in vivo*.[292–294] However, the translation of this technology for human use has been stalled by difficulties targeting the nanoparticles to the tumor[295] since many gold nanoparticles rely solely on the enhanced permeation and retention effect of tumors to increase uptake relative to healthy tissues. As an alternative to gold, hafnium-based nanoparticles are currently being investigated in clinical trials.[296] Although less work has been done to investigate the quantification of these particles using DECT, there is some evidence that it is possible,[297] and hafnium, with a K-edge of 65.4 keV, may be a candidate for K-edge imaging with PCD-CT. Should these particles make it to clinical applications, DECT and PCD-CT could play an important role in quantifying the distribution in the tumor for advanced radiation treatment planning.

4.C. Image-guided intervention applications

There are many opportunities for development of quantitative CT applications for image-guided therapy. Transcatheter arterial chemoembolization (TACE) is a treatment modality primarily for liver tumors in which an interventional radiologist injects chemotherapeutic and embolic agents directly into a tumor’s blood supply under image guidance. In order to visualize the treatment delivery, the chemotherapeutic agent is emulsified with a small amount of lipiodol (iodinated poppy seed oil) prior to injection,[298–300] and the embolization is considered successful if there is complete lipiodol uptake in the tumor without arterial enhancement in the tumor on CT acquired one month post-treatment. One major disadvantage of using lipiodol for TACE monitoring is that the high attenuation of the lipiodol makes it difficult to assess the residual vascularity of tumors with angiography immediately following treatment. In-room DECT or PCD-CT would allow for acquisition of CT angiography using alternative contrast agents that could be separated from the lipiodol using material decomposition algorithms and application of new theranostic agents.

Separation of the TACE drug from the lipiodol following injection is one concern for this paradigm. Tagging the chemotherapeutic agent directly with a highly attenuating material such as bismuth, tungsten, or ytterbium could allow for direct tracking of the drug, and could also be applied to drug-eluting particle therapies. In a recent article by Sofue et al. multi-energy CT was used to quantify the concentration of cisplatin, a platinum-based chemotherapeutic agent, in the presence of iodine using phantoms and a three-material decomposition of cisplatin, iodine, and agar.[301] While this has not yet been tested in patients, the study demonstrates that drugs containing high-Z materials with dual-energy ratios significantly different from iodine can be identified on imaging using DECT. This effect could be further exploited using K-edge imaging with PCD-CT by tagging drugs with nanoparticle contrast agents. This will enable visualization of the actual patient-specific biodistribution within the tumor, quantification of drug delivery to the tumor and evaluation of new drug-eluting medical devices for pharmacokinetics.

5. DISCUSSION

The use of imaging in medicine has largely been limited to qualitative assessments of anatomy and disease processes. Quantitative CT can play a large part in reducing the subjectivity of imaging interpretation moving forward. Examples of this include bone mineral density assessment, which is increasingly performed on an opportunistic basis with CT, and the use of CT number thresholds for diagnosis, as seen in conventional imaging for hepatic steatosis. Even RECIST criteria can suffer from physician bias in the determination of tumor diameters, and fatty infiltration of the liver may not be uniform and so ROI-based assessments may not characterize the whole liver. A current gap in knowledge is the impact of specific acquisition and reconstruction parameters on quantitative imaging results. Therefore, in addition to the development of new quantitative metrics, there must be steps taken to automate and standardize the way measurements are gathered for particular disease profiles. While this is beginning to be addressed in the field of radiomics,[197] it typically has not been assessed for DECT-based quantification methods. This must be performed on both a small scale (e.g., parameters at a given institution) and large scale (e.g., comparisons between vendors/platforms and multi-institutional studies). Broader standardization of imaging protocols across institutions can help to minimize variability in interpretation and quantitative results, and can be used to better inform clinicians about relevant biological processes. However, there remain barriers to the inclusion of such quantitative information, including the need for structured reporting of data and development of workflows for quantitative analysis.

Photon-counting detector CT is the most recent CT hardware technology to be developed, and human prototypes are now available at select academic centers around the world. The energy resolution of the detector enables better identification and quantification of novel materials, and spatial resolution is greatly improved over conventional CT. These advancements can assist with the characterization of tumors, atherosclerotic plaques, and abnormal vasculature. As this is largely a new topic in the field of medical imaging, there are many opportunities for advancement and application development to prepare the technology for clinical use. Photon-counting detector CT spectral distortions from nonideal detector performance currently minimize the potential advantages of these systems over

DECT spectral acquisition, but developing corrections for the spectrum is an active area of research. There are multiple detector technologies available, and comparisons between them will need to be performed as systems are released commercially. Additional reconstruction parameters and image types must be optimized for specific imaging protocols, including the number and spacing of energy bins based on both the contrast agents utilized and the noise profile within each bin that is tolerable for visualization, material decomposition, and quantification. Applications currently may require development in large animal models, cadaver studies, or phantom experiments in order to translate them from the bench to the bedside. The impact of larger image matrices to accommodate the system resolution requires evaluation, and as contrast agents are developed, each will need to undergo clinical trials for safety and efficacy. As with the adoption of DECT, there must also be a significant effort to educate physicians about the differences in expected image characteristics between conventional and PCD-CT, such as reduced image noise and increased spatial resolution.

While development of novel tracers is common for nuclear medicine modalities, there has been very little focus on the use of new CT contrast agents until the development of PCD-CT. Clinical iodinated contrast agents are unable to be targeted in their current form, and therefore do not provide the diagnostic specificity that targeted tracers may be capable of achieving. Unique CT tracers would be particularly valuable for oncologic imaging, as they could enable enhanced detection of both primary tumors and distant metastases, with the potential for improving detection of smaller metastases than would be feasible with conventional CT. Subsequently, there could be improved delineation of gross target volumes in radiotherapy to include additional microscopic disease. In oncology, patients typically receive follow-up imaging every 3–6 months, and DECT has already had a positive impact on monitoring treatment response for many patients during their care, but innovative contrast agents could potentially provide additional and specific diagnostic information to clinicians regarding the characteristics of tumor heterogeneity, the tumor microenvironment, or associated immune and inflammatory responses. The nanoparticle contrast agents described in Section 5.A can all be readily adapted to this new imaging paradigm. However, the majority of novel contrast agents are being developed for use with PCD-CT and have K-edges between 40 and 100 keV, which is disallowed by the assumptions of currently available DECT material decomposition algorithms. In addition to limited applicability to current scanner technology, targeted contrast agents may only be present within diseased tissue in very small quantities. Therefore, high PCD-CT sensitivity is paramount in order to detect these agents and may depend on parameters such as the number of energy bins and the binning of pixels within the detector, and will be an ongoing area of interest as more human PCD-CT prototypes are made available.

6. CONCLUSIONS

The advancements in multi-energy CT demonstrate exciting opportunities for quantitative imaging. This is imperative, as there is a critical need to improve characterization and response assessment of disease and subsets of diseases. Realization of additional enhancements are conceivable with the development of new, targeted contrast agents along with high-resolution material-specific imaging (e.g. PCD-CT K-edge) to further improve specificity and potential new applications, especially translation to image-guided therapy and interventions. Current challenges in quantitative imaging, such as limited assessment of protocol-induced variability in metrics, provide unique opportunities for medical physicists to become involved in translational research, provide physician education, and impact patient care. In summary, the technical advancements of quantitative multi-energy CT provides numerous opportunities for advancement related to biology, drug development and medical subspecialties to help reduce variability in interpretation, and provide valuable insight to physicians and patients.

ACKNOWLEDGMENTS

The authors like to acknowledge the following funding sources: the National Institute of Biomedical Imaging and Bioengineering (R01EB016966), the National Cancer Institute (R01CA201127, R01CA221971, and R21CA216572), National Institutes of Health Cancer Center Support Grant P30CA016672, the National Aeronautics and Space Administration (80NSSC18K1639), and the Helen Black Image Guidance Fund. The content is solely the responsibility of the authors and does not necessarily represent the official views of the National Institutes of Health or other institutions.

CONFLICT OF INTEREST

Rick Layman receives research funding from Siemens Healthineers and General Electric Healthcare. Dianna Cody has a consulting agreement with Gammex (Sun Nuclear). Eric Tamm receives in-kind support from General Electric Healthcare. Kristy Brock has a licensing agreement with Ray-Search Laboratories and receives research funding from Ray-Search and the National Cancer Institute. Laurence Court receives funding from Varian Medical Systems. The remaining authors have no relevant conflicts of interest to disclose.

REFERENCES

1. Kim SH, Kamaya A, Willmann JK. CT perfusion of the liver: principles and applications in oncology. Radiology. 2014;272:322–344. [PubMed: 25058132]
2. Konstas AA, Goldmakher GV, Lee TY, Lev MH. Theoretic basis and technical implementations of CT perfusion in acute ischemic stroke, part 1: theoretic basis. Am J Neuroradiol. 2009;30:662–668. [PubMed: 19270105]
3. Konstas AA, Goldmakher GV, Lee TY, Lev MH. Theoretic basis and technical implementations of CT perfusion in acute ischemic stroke, part 2: technical implementations. Am J Neuroradiol. 2009;30:885–892. [PubMed: 19299489]
4. Pullan BR, Fawcitt RA, Isherwood I. Tissue characterization by an analysis of the distribution of attenuation values in computed tomography scans: a preliminary report. J Comput Assist Tomogr. 1978;2:49–54. [PubMed: 670471]
5. Norman D, Price D, Boyd D, Fishman R, Newton TH. Quantitative aspects of computed tomography of the blood and cerebrospinal fluid. Radiology. 1977;123:335–338. [PubMed: 847198]
6. Huckman MS, Ackerman LV. Use of automated measurements of mean density as an adjunct to computed tomography. J Comput Assist Tomogr. 1977;1:37–42. [PubMed: 615892]
7. Genant HK, Boyd D. Quantitative bone mineral analysis using dual energy computed tomography. Invest Radiol. 1977;12:545–551. [PubMed: 591258]
8. Exner GU, Prader A, Elsasser U, Ruegsegger P, Anliker M. Bone densitometry using computed tomography. Part I: selective determination of trabecular bone density and other bone mineral parameters. Normal values in children and adults. Br J Radiol. 1979;52:14–23. [PubMed: 427345]
9. Cann CE, Genant HK, Ettinger B, Gordan GS. Spinal mineral loss in oophorectomized women. Determination by quantitative computed tomography. JAMA. 1980;244:2056–2059. [PubMed: 6253692]
10. Jensen PS, Orphanoudakis SC, Rauschkolb EN, Baron R, Lang R, Rasmussen H. Assessment of bone mass in the radius by computed tomography. AJR Am J Roentgenol. 1980;134:285–292. [PubMed: 6766235]

11. Weissberger MA, Zamenhof RG, Aronow S, Neer RM. Computed tomography scanning for the measurement of bone mineral in the human spine. J Comput Assist Tomogr. 1978;2:253–262. [PubMed: 263488]
12. Reinbold WD, Genant HK, Reiser UJ, Harris ST, Ettinger B. Bone mineral content in early-postmenopausal and postmenopausal osteoporotic women: comparison of measurement methods. Radiology. 1986;160:469–478. [PubMed: 3726129]
13. Ruegsegger P, Elsasser U, Anliker M, Gnehm H, Kind H, Prader A. Quantification of bone mineralization using computed tomography. Radiology. 1976;121:93–97. [PubMed: 959563]
14. Liliequist B, Wirell S. Quantitative estimation of tumor volume on computer assisted tomography. J Comput Assist Tomogr. 1978;2:300–302. [PubMed: 263494]
15. Quivey JM, Castro JR, Chen GT, Moss A, Marks WM. Computerized tomography in the quantitative assessment of tumour response. Br J Cancer Suppl. 1980;4:30–34. [PubMed: 6932941]
16. Go JL, Zee CS. Unique CT imaging advantages. Hemorrhage and calcification. Neuroimaging Clin N Am. 1998;8:541–558. [PubMed: 9673312]
17. Bockenheimer S. Diagnostic and interventional neuroradiology: a multimodality approach. In: Sartor K, ed. Stuttgart. New York: Thieme; 2002:160–169.
18. Israel GM, Bosniak MA. How i do it: evaluating renal masses. Radiology. 2005;236:441–450. [PubMed: 16040900]
19. Bosniak MA. The current radiological approach to renal cysts. Radiology. 1986;158:1–10. [PubMed: 3510019]
20. Israel GM, Bosniak MA. An update of the Bosniak renal cyst classification system. Urology. 2005;66:484–488. [PubMed: 16140062]
21. Bertolotto M, Cicero C, Perrone R, Degrassi F, Cacciato F, Cova MA. Renal masses with equivocal enhancement at CT: characterization with contrast-enhanced ultrasound. AJR Am J Roentgenol. 2015;204:W557–W565. [PubMed: 25905962]
22. The Joint Commission. Comprehensive Accreditation Manual for Hospitals: The Official Handbook. In: Environment of Care. Vol 20–21; 2019.
23. Hounsfield GN. Computerized transverse axial scanning (tomography): part 1. Description of system. Br J Radiol. 1973;46:1016–1022. [PubMed: 4757352]
24. Alvarez RE, Macovski A. Energy-selective reconstructions in X-ray computerized tomography. Phys Med Biol. 1976;21:733–744. [PubMed: 967922]
25. Johnson TR, Krauss B, Sedlmair M, et al. Material differentiation by dual energy CT: initial experience. Eur Radiol. 2007;17:1510–1517. [PubMed: 17151859]
26. Macovski A, Alvarez RE, Chan JL, Stonestrom JP, Zatz LM. Energy dependent reconstruction in X-ray computerized tomography. Comput Biol Med. 1976;6:325–336. [PubMed: 1000958]
27. Yu L, Leng S, McCollough CH. Dual-energy CT-based monochromatic imaging. AJR Am J Roentgenol. 2012;199:S9–S15. [PubMed: 23097173]
28. Schlomka JP, Roessl E, Dorscheid R, et al. Experimental feasibility of multi-energy photon-counting K-edge imaging in pre-clinical computed tomography. Phys Med Biol. 2008;53:4031–4047. [PubMed: 18612175]
29. Anderson NG, Butler AP, Scott NJ, et al. Spectroscopic (multi-energy) CT distinguishes iodine and barium contrast material in MICE. Eur Radiol. 2010;20:2126–2134. [PubMed: 20309554]
30. Yu Z, Leng S, Jorgensen SM, et al. Evaluation of conventional imaging performance in a research whole-body CT system with a photon-counting detector array. Phys Med Biol. 2016;61:1572–1595. [PubMed: 26835839]
31. Pourmorteza A, Symons R, Sandfort V, et al. Abdominal imaging with contrast-enhanced photon-counting CT: first human experience. Radiology. 2016;279:239–245. [PubMed: 26840654]
32. Leng S, Zhou W, Yu Z, et al. Spectral performance of a whole-body research photon counting detector CT: quantitative accuracy in derived image sets. Phys Med Biol. 2017;62:7216–7232. [PubMed: 28726669]
33. Persson M, Huber B, Karlsson S, et al. Energy-resolved CT imaging with a photon-counting silicon-strip detector. Phys Med Biol. 2014;59:6709–6727. [PubMed: 25327497]

34. Leng S, Rajendran K, Gong H, et al. 150-lm spatial resolution using photon-counting detector computed tomography technology: technical performance and first patient images. Invest Radiol. 2018;53: 655–662. [PubMed: 29847412]
35. Tao S, Rajendran K, McCollough CH, Leng S. Feasibility of multi-contrast imaging on dual-source photon counting detector (PCD) CT: An initial phantom study. Med Phys. 2019;46:4105–4155. [PubMed: 31215659]
36. Leng S, Bruesewitz M, Tao S, et al. Photon-counting detector CT: system design and clinical applications of an emerging technology. Radiographics. 2019;39:729–743. [PubMed: 31059394]
37. Symons R, Krauss B, Sahbaee P, et al. Photon-counting CT for simultaneous imaging of multiple contrast agents in the abdomen: an in vivo study. Med Phys. 2017;44:5120–5127. [PubMed: 28444761]
38. Yu Z, Leng S, Kappler S, et al. Noise performance of low-dose CT: comparison between an energy integrating detector and a photon counting detector using a whole-body research photon counting CT scanner. J Med Imaging (Bellingham). 2016;3:043503. [PubMed: 28018936]
39. Fredette NR, Kavuri A, Das M. Multi-step material decomposition for spectral computed tomography. Phys Med Biol. 2019;64:145001. [PubMed: 31216514]
40. Muenzel D, Bar-Ness D, Roessl E, et al. Spectral photon-counting CT: initial experience with dual-contrast agent K-edge colonography. Radiology. 2017;283:723–728. [PubMed: 27918709]
41. Curtis TE, Roeder RK. Quantification of multiple mixed contrast and tissue compositions using photon-counting spectral computed tomography. J Med Imaging (Bellingham). 2019;6:013501. [PubMed: 30840726]
42. QIBA CT Volumetry Technical Committee. CT Tumor Volume Change Profile - 2018, Technically Confirmed Profile. Quantitative Imaging Biomarkers Alliance; 6 22, 2018; 2018.
43. QIBA CT Volumetry Technical Committee. Small Lung Nodule Assessment in CT Screening Profile - 2018. Quantitative Imaging Biomarkers Alliance; 2018.
44. Miller AB, Hoogstraten B, Staquet M, Winkler A. Reporting results of cancer treatment. Cancer. 1981;47:207–214. [PubMed: 7459811]
45. Therasse P, Arbuck SG, Eisenhauer EA, et al. New guidelines to evaluate the response to treatment in solid tumors. European Organization for Research and Treatment of Cancer, National Cancer Institute of the United States, National Cancer Institute of Canada. J Natl Cancer Inst. 2000;92:205–216. [PubMed: 10655437]
46. Eisenhauer EA, Therasse P, Bogaerts J, et al. New response evaluation criteria in solid tumours: revised RECIST guideline (version 1.1). Eur J Cancer. 2009;45:228–247. [PubMed: 19097774]
47. Choi H, Charnsangavej C, Faria SC, et al. Correlation of computed tomography and positron emission tomography in patients with metastatic gastrointestinal stromal tumor treated at a single institution with imatinib mesylate: proposal of new computed tomography response criteria. J Clin Oncol. 2007;25:1753–1759. [PubMed: 17470865]
48. Benjamin RS, Choi H, Macapinlac HA, et al. We should desist using RECIST, at least in GIST. J Clin Oncol. 2007;25:1760–1764. [PubMed: 17470866]
49. Nathan PD, Vinayan A, Stott D, Juttla J, Goh V. CT response assessment combining reduction in both size and arterial phase density correlates with time to progression in metastatic renal cancer patients treated with targeted therapies. Cancer Biol Ther. 2010;9:15–19. [PubMed: 20009542]
50. Wright NC, Saag KG, Dawson-Hughes B, Khosla S, Siris ES. The impact of the new National Bone Health Alliance (NBHA) diagnostic criteria on the prevalence of osteoporosis in the USA. Osteopor Int. 2017;28:1225–1232.
51. Curtis EM, Moon RJ, Harvey NC, Cooper C. The impact of fragility fracture and approaches to osteoporosis risk assessment worldwide. Bone. 2017;104:29–38. [PubMed: 28119181]
52. Burge R, Dawson-Hughes B, Solomon DH, Wong JB, King A, Tosteson A. Incidence and economic burden of osteoporosis-related fractures in the United States, 2005–2025. J Bone Miner Res. 2007;22:465–475. [PubMed: 17144789]
53. Carter DR, Bouxsein ML, Marcus R. New approaches for interpreting projected bone densitometry data. J Bone Miner Res. 1992;7:137–145. [PubMed: 1570758]
54. Nelson L, Gulenchyn KY, Atthey M, Webber CE. Is a fixed value for the least significant change appropriate? J Clin Densitom. 2010;13:18–23. [PubMed: 20171565]

55. Van Loan MD, Johnson HL, Barbieri TF. Effect of weight loss on bone mineral content and bone mineral density in obese women. Am J Clin Nutr. 1998;67:734–738. [PubMed: 9537621]

56. Tothill P. Dual-energy x-ray absorptiometry measurements of total-body bone mineral during weight change. J Clin Densitom. 2005;8:31–38. [PubMed: 15722585]

57. Yu EW, Thomas BJ, Brown JK, Finkelstein JS. Simulated increases in body fat and errors in bone mineral density measurements by DXA and QCT. J Bone Miner Res. 2011;27:119–124.

58. Tothill P, Weir N, Loveland J. Errors in dual-energy X-ray scanning of the hip because of nonuniform fat distribution. J Clin Densitom. 2014;17:91–96. [PubMed: 23522983]

59. Bolotin HH. DXA in vivo BMD methodology: an erroneous and misleading research and clinical gauge of bone mineral status, bone fragility, and bone remodelling. Bone. 2007;41:138–154. [PubMed: 17481978]

60. Gafni RI, Baron J. Overdiagnosis of osteoporosis in children due to misinterpretation of Dual-energy x-ray absorptiometry (DEXA). J Pediatr. 2004;144:253–257. [PubMed: 14760271]

61. Rand T, Seidl G, Kainberger F, et al. Impact of spinal degenerative changes on the evaluation of bone mineral density with dual energy X-ray absorptiometry (DXA). Calcif Tissue Int. 1997;60:430–433. [PubMed: 9115160]

62. Yu W, Gluer CC, Fuerst T, et al. Influence of degenerative joint disease on spinal bone mineral measurements in postmenopausal women. Calcif Tissue Int. 1995;57:169–174. [PubMed: 8574931]

63. Cann CE, Genant HK. Precise measurement of vertebral mineral content using computed tomography. J Comput Assist Tomogr. 1980;4:493–500. [PubMed: 7391292]

64. Kalender WA, Klotz E, Suess C. Vertebral bone mineral analysis: an integrated approach with CT. Radiology. 1987;164:419–423. [PubMed: 3602380]

65. Wang L, Su Y, Wang Q et al. Validation of asynchronous quantitative bone densitometry of the spine: accuracy, short-term reproducibility, and a comparison with conventional quantitative computed tomography. Sci Rep. 2017;7:6284. [PubMed: 28740145]

66. Lee DC, Hoffmann PF, Kopperdahl DL, Keaveny TM. Phantomless calibration of CT scans for measurement of BMD and bone strength-Inter-operator reanalysis precision. Bone. 2017;103:325–333. [PubMed: 28778598]

67. Gudmundsdottir H, Jonsdottir B, Kristinsson S, Johannesson A, Good-enough D, Sigurdsson G. Vertebral bone density in icelandic women using quantitative computed tomography without an external reference phantom. Osteoporos Int. 1993;3:84–89. [PubMed: 8453195]

68. Emohare O, Dittmer A, Morgan RA, Switzer JA, Polly DW Jr. Osteoporosis in acute fractures of the cervical spine: the role of opportunistic CT screening. J Neurosurg Spine. 2015;23:1–7. [PubMed: 25860516]

69. Lee SJ, Binkley N, Lubner MG, Bruce RJ, Ziemlewicz TJ, Pickhardt PJ. Opportunistic screening for osteoporosis using the sagittal reconstruction from routine abdominal CT for combined assessment of vertebral fractures and density. Osteoporos Int. 2016;27:1131–1136. [PubMed: 26419470]

70. Garner HW, Paturzo MM, Gaudier G, Pickhardt PJ, Wessell DE. Variation in attenuation in L1 trabecular bone at different tube voltages: caution is warranted when screening for osteoporosis with the use of opportunistic CT. AJR Am J Roentgenol. 2016;208:165–170. [PubMed: 27762605]

71. Cann CE, Adams JE, Brown JK, Brett AD. CTXA hip–an extension of classical DXA measurements using quantitative CT. PLoS One. 2014;9: e91904. [PubMed: 24637515]

72. Fidler JL, Murthy NS, Khosla S, et al. Comprehensive assessment of osteoporosis and bone fragility with CT colonography. Radiology. 2015;278:172–180. [PubMed: 26200602]

73. Bousson V, Le Le BA, Roqueplan F, et al. Volumetric quantitative computed tomography of the proximal femur: relationships linking geometric and densitometric variables to bone strength. Role for compact bone. Osteoporos Int. 2006;17:855–864. [PubMed: 16547689]

74. American College of Radiology, Society of Pediatric Radiology, Society of Skeletal Radiology. ACR-SPR-SSR Practice Parameter for the Performance of Musculoskeletal Quantitative Computed Tomography (QCT); 2018:14. https://acsearch.acr.org/docs/70546/Narrative/. Accessed October 26, 2018.

75. Richelson LS, Wahner HW, Melton LJ, Riggs BL. Relative contributions of aging and estrogen deficiency to postmenopausal bone loss. N Engl J Med. 1984;311:1273–1275. [PubMed: 6493283]
76. Ahlborg HG, Johnell O, Turner CH, Rannevik G, Karlsson MK. Bone loss and bone size after menopause. N Engl J Med. 2003;349:327–334. [PubMed: 12878739]
77. Adams JE. Quantitative computed tomography. Eur J Radiol. 2009;71:415–424. [PubMed: 19682815]
78. Vetter JR, Perman WH, Kalender WA, Mazess RB, Holden JE. Evaluation of a prototype dual-energy computed tomographic apparatus. II. Determination of vertebral bone mineral content. Med Phys. 1986;13:340–343. [PubMed: 3724694]
79. Kalender WA, Felsenberg D, Louis O, et al. Reference values for trabecular and cortical vertebral bone density in single and dual-energy quantitative computed tomography. Eur J Radiol. 1989;9:75–80. [PubMed: 2743986]
80. Nickoloff EL, Feldman F, Atherton JV. Bone mineral assessment: new dual-energy CT approach. Radiology. 1988;168:223–228. [PubMed: 3380964]
81. Mazess RB. Errors in measuring trabecular bone by computed tomography due to marrow and bone composition. Calcif Tissue Int. 1983;35:148–152. [PubMed: 6850397]
82. Arentsen L, Hansen KE, Yagi M, et al. Use of dual-energy computed tomography to measure skeletal-wide marrow composition and cancellous bone mineral density. J Bone Miner Metab. 2017;35:428–436. [PubMed: 27942979]
83. Hofmann P, Sedlmair M, Krauss B, et al. Phantom-less bone mineral density (BMD) measurement using dual energy computed tomography-based 3-material decomposition. Paper presented at: SPIE Medical Imaging; 2016.
84. Wesarg S, Kirschner M, Becker M, Erdt M, Kafchitsas K, Khan MF. Dual-energy CT-based assessment of the trabecular bone in vertebrae. Methods Inf Med. 2012;51:398–405. [PubMed: 23038636]
85. Wait JM, Cody D, Jones AK, Rong J, Baladandayuthapani V, Kappa-dath SC. Performance evaluation of material decomposition with rapid-kilovoltage-switching dual-energy CT and implications for assessing bone mineral density. AJR Am J Roentgenol. 2015;204:1234–1241. [PubMed: 26001233]
86. Van Hedent S, Su KH, Jordan DW, et al. Improving bone mineral density assessment using spectral detector CT. J Clin Densitom. 2018;22:374–381. [PubMed: 30497869]
87. Younossi ZM, Koenig AB, Abdelatif D, Fazel Y, Henry L, Wymer M. Global epidemiology of nonalcoholic fatty liver disease-Meta-analytic assessment of prevalence, incidence, and outcomes. Hepatology. 2016;64:73–84. [PubMed: 26707365]
88. Fuster D, Samet JH. Alcohol use in patients with chronic liver disease. N Engl J Med. 2018;379:1251–1261. [PubMed: 30257164]
89. Abenavoli L, Masarone M, Peta V, et al. Insulin resistance and liver steatosis in chronic hepatitis C infection genotype 3. World J Gastroenterol. 2014;20:15233–15240. [PubMed: 25386071]
90. Shigefuku R, Takahashi H, Nakano H, et al. Correlations of hepatic hemodynamics, liver function, and fibrosis markers in nonalcoholic fatty liver disease: comparison with chronic hepatitis related to hepatitis C virus. Int J Mol Sci. 2016;17:1545.
91. Satapathy SK, Kuwajima V, Nadelson J, Atiq O, Sanyal AJ. Drug-induced fatty liver disease: an overview of pathogenesis and management. Ann Hepatol. 2015;14:789–806. [PubMed: 26436351]
92. Ogawa Y, Murata Y, Nishioka A, Inomata T, Yoshida S. Tamoxifen-induced fatty liver in patients with breast cancer. Lancet. 1998;351:725.
93. Wakatsuki A, Ogawa Y, Saibara T, Okatani Y, Fukaya T. Size and oxidative susceptibility of low-density lipoprotein particles in breast cancer patients with tamoxifen-induced fatty liver. J Clin Endocrinol Metab. 2002;87:3676–3681. [PubMed: 12161495]
94. Woods CP, Hazlehurst JM, Tomlinson JW. Glucocorticoids and non-alcoholic fatty liver disease. J Steroid Biochem Mol Biol. 2015;154: 94–103. [PubMed: 26241028]
95. Alberti KG, Eckel RH, Grundy SM, et al. Harmonizing the metabolic syndrome: a joint interim statement of the International Diabetes Federation Task Force on Epidemiology and Prevention; National Heart, Lung, and Blood Institute; American Heart Association; World Heart Federation;

International Atherosclerosis Society; and International Association for the Study of Obesity. Circulation. 2009;120:1640–1645. [PubMed: 19805654]

96. Marchesini G, Bugianesi E, Forlani G, et al. Nonalcoholic fatty liver, steatohepatitis, and the metabolic syndrome. Hepatology. 2003;37: 917–923. [PubMed: 12668987]
97. Caldwell SH, Crespo DM. The spectrum expanded: cryptogenic cirrhosis and the natural history of non-alcoholic fatty liver disease. J Hepatol. 2004;40:578–584. [PubMed: 15030972]
98. Caldwell SH, Oelsner DH, Iezzoni JC, Hespenheide EE, Battle EH, Driscoll CJ. Cryptogenic cirrhosis: clinical characterization and risk factors for underlying disease. Hepatology. 1999;29:664–669. [PubMed: 10051466]
99. Degasperi E, Colombo M. Distinctive features of hepatocellular carcinoma in non-alcoholic fatty liver disease. Lancet Gastroenterol Hepatol. 2016;1:156–164. [PubMed: 28404072]
100. Yasui K, Hashimoto E, Komorizono Y, et al. Characteristics of patients with nonalcoholic steatohepatitis who develop hepatocellular carcinoma. Clin Gastroenterol Hepatol. 2011;9:428–433. [PubMed: 21320639]
101. Su CW, Chau GY, Hung HH, et al. Impact of steatosis on prognosis of patients with early-stage hepatocellular carcinoma after hepatic resection. Ann Surg Oncol. 2015;22:2253–2261. [PubMed: 25490872]
102. d'Assignies G, Fayard C, Leitao H, et al. Liver steatosis assessed by preoperative MRI: an independent risk factor for severe complications after major hepatic resection. Surgery. 2016;159:1050–1057. [PubMed: 26582502]
103. Reddy SK, Marsh JW, Varley PR, et al. Underlying steatohepatitis, but not simple hepatic steatosis, increases morbidity after liver resection: a case-control study. Hepatology. 2012;56:2221–2230. [PubMed: 22767263]
104. Boll DT, Marin D, Redmon GM, Zink SI, Merkle EM. Pilot study assessing differentiation of steatosis hepatis, hepatic iron overload, and combined disease using two-point dixon MRI at 3 T: in vitro and in vivo results of a 2D decomposition technique. AJR Am J Roentgenol. 2010;194:964–971. [PubMed: 20308498]
105. Fischer MA, Raptis DA, Montani M, et al. Liver fat quantification by dual-echo MR imaging outperforms traditional histopathological analysis. Acad Radiol. 2012;19:1208–1214. [PubMed: 22841289]
106. Kuhn JP, Evert M, Friedrich N, et al. Noninvasive quantification of hepatic fat content using three-echo dixon magnetic resonance imaging with correction for T2* relaxation effects. Invest Radiol. 2011;46:783–789. [PubMed: 21808200]
107. Kukuk GM, Hittatiya K, Sprinkart AM, et al. Comparison between modified Dixon MRI techniques, MR spectroscopic relaxometry, and different histologic quantification methods in the assessment of hepatic steatosis. Eur Radiol. 2015;25:2869–2879. [PubMed: 25903702]
108. Longo R, Pollesello P, Ricci C, et al. Proton MR spectroscopy in quantitative in vivo determination of fat content in human liver steatosis. J Magn Reson Imaging. 1995;5:281–285. [PubMed: 7633104]
109. Bannas P, Kramer H, Hernando D, et al. Quantitative magnetic resonance imaging of hepatic steatosis: validation in ex vivo human livers. Hepatology. 2015;62:1444–1455. [PubMed: 26224591]
110. Longo R, Ricci C, Masutti F, et al. Fatty infiltration of the liver. Quantification by 1H localized magnetic resonance spectroscopy and comparison with computed tomography. Invest Radiol. 1993;28:297–302. [PubMed: 8478169]
111. Hamer OW, Aguirre DA, Casola G, Lavine JE, Woenckhaus M, Sirlin CB. Fatty liver: imaging patterns and pitfalls. Radiographics. 2006;26:1637–1653. [PubMed: 17102041]
112. Kodama Y, Ng CS, Wu TT, et al. Comparison of CT methods for determining the fat content of the liver. AJR Am J Roentgenol. 2007;188:1307–1312. [PubMed: 17449775]
113. Ricci C, Longo R, Gioulis E, et al. Noninvasive in vivo quantitative assessment of fat content in human liver. J Hepatol. 1997;27:108–113. [PubMed: 9252082]
114. Pickhardt PJ, Graffy PM, Reeder SB, Hernando D, Li K. Quantification of liver fat content with unenhanced MDCT: phantom and clinical correlation with MRI proton density fat fraction. AJR Am J Roentgenol. 2018;211:W151–W157. [PubMed: 30016142]

115. Joy D, Thava VR, Scott BB. Diagnosis of fatty liver disease: is biopsy necessary? Eur J Gastroenterol Hepatol. 2003;15:539–543. [PubMed: 12702913]

116. Piekarski J, Goldberg HI, Royal SA, Axel L, Moss AA. Difference between liver and spleen CT numbers in the normal adult: its usefulness in predicting the presence of diffuse liver disease. Radiology. 1980;137:727–729. [PubMed: 6934563]

117. Limanond P, Raman SS, Lassman C, et al. Macrovesicular hepatic steatosis in living related liver donors: correlation between CT and histologic findings. Radiology. 2004;230:276–280. [PubMed: 14695401]

118. Kramer H, Pickhardt PJ, Kliewer MA, et al. Accuracy of liver fat quantification with advanced CT, MRI, and ultrasound techniques: prospective comparison with MR spectroscopy. AJR Am J Roentgenol. 2016;208:92–100. [PubMed: 27726414]

119. Artz NS, Hines CDG, Brunner ST, et al. Quantification of hepatic steatosis with dual-energy computed tomography: comparison with tissue reference standards and quantitative magnetic resonance imaging in the ob/ob mouse. Invest Radiol. 2012;47:603–610. [PubMed: 22836309]

120. Mendonca PR, Lamb P, Sahani DV. A flexible method for multi-material decomposition of dual-energy CT Images. IEEE Trans Med Imaging. 2014;33:99–116. [PubMed: 24058018]

121. Hyodo T, Hori M, Lamb P, et al. Multimaterial decomposition algorithm for the quantification of liver fat content by using fast-kilovolt-peak Switching dual-energy CT: experimental validation. Radiology. 2016;282:381–389. [PubMed: 27541687]

122. Hyodo T, Yada N, Hori M, et al. Multimaterial decomposition algorithm for the quantification of liver fat content by using fast-kilovolt-peak switching dual-energy CT: clinical evaluation. Radiology. 2017;283:108–118. [PubMed: 28212047]

123. Morgan DE, Weber AC, Lockhart ME, Weber TM, Fineberg NS, Berland LL. Differentiation of high lipid content from low lipid content adrenal lesions using single-source rapid kilovolt (peak)-switching dual-energy multidetector CT. J Comput Assist Tomogr. 2013;37: 937–943. [PubMed: 24270116]

124. Mileto A, Nelson RC, Marin D, Roy Choudhury K, Ho LM. Dual-energy multidetector CT for the characterization of incidental adrenal nodules: diagnostic performance of contrast-enhanced material density analysis. Radiology. 2015;274:445–454. [PubMed: 25207467]

125. Fischer MA, Reiner CS, Raptis D, et al. Quantification of liver iron content with CT—added value of dual-energy. Eur Radiol. 2011;21: 1727–1732. [PubMed: 21472472]

126. Fischer MA, Gnannt R, Raptis D, et al. Quantification of liver fat in the presence of iron and iodine: an ex-vivo dual-energy CT study. Invest Radiol. 2011;46:351–358. [PubMed: 21263329]

127. Ma J, Song Z-Q, Yan F-H. Separation of hepatic iron and fat by dual-source dual-energy computed tomography based on material decomposition: an animal study. PLoS One. 2014;9:e110964. [PubMed: 25356845]

128. Siegel RL, Miller KD, Jemal A. Cancer statistics, 2018. CA Cancer J Clin. 2018;68:7–30. [PubMed: 29313949]

129. Berland LL, Silverman SG, Gore RM, et al. Managing incidental findings on abdominal CT: white paper of the ACR incidental findings committee. J Am Coll Radiol. 2010;7:754–773. [PubMed: 20889105]

130. Patard JJ, Leray E, Rioux-Leclercq N, et al. Prognostic value of histologic subtypes in renal cell carcinoma: a multicenter experience. J Clin Oncol. 2005;23:2763–2771. [PubMed: 15837991]

131. Storkel S, van den Berg E. Morphological classification of renal cancer. World J Urol. 1995;13:153–158. [PubMed: 7550386]

132. Kim SH, Kim CS, Kim MJ, Cho JY, Cho SH. Differentiation of clear cell renal cell carcinoma from other subtypes and fat-poor angiomyolipoma by use of quantitative enhancement measurement during three-phase MDCT. AJR Am J Roentgenol. 2015;206:W21–W28.

133. Yang C-W, Shen S-H, Chang Y-H, et al. Are there useful CT features to differentiate renal cell carcinoma from lipid-poor renal angiomyolipoma? AJR Am J Roentgenol. 2013;201:1017–1028. [PubMed: 24147472]

134. Sasaguri K, Takahashi N, Gomez-Cardona D, et al. Small (< 4 cm) renal mass: differentiation of oncocytoma from renal cell carcinoma on biphasic contrast-enhanced CT. AJR Am J Roentgenol. 2015;205: 999–1007. [PubMed: 26496547]

135. Hodgdon T, McInnes MDF, Schieda N, Flood TA, Lamb L, Thornhill RE. Can quantitative CT texture analysis be used to differentiate fat-poor renal angiomyolipoma from renal cell carcinoma on unenhanced CT Images? Radiology. 2015;276:787–796. [PubMed: 25906183]
136. Kaza RK, Caoili EM, Cohan RH, Platt JF. Distinguishing enhancing from nonenhancing renal lesions with fast kilovoltage-switching dual-energy CT. AJR Am J Roentgenol. 2011;197:1375–1381. [PubMed: 22109292]
137. Mileto A, Marin D, Ramirez-Giraldo JC, et al. Accuracy of contrast-enhanced dual-energy MDCT for the assessment of iodine uptake in renal lesions. AJR Am J Roentgenol. 2014;202:W466–W474. [PubMed: 24758682]
138. Chandarana H, Megibow AJ, Cohen BA, et al. Iodine quantification with dual-energy CT: phantom study and preliminary experience with renal masses. AJR Am J Roentgenol. 2011;196:W693–W700. [PubMed: 21606256]
139. Primak AN, Fletcher JG, Vrtiska TJ, et al. Noninvasive differentiation of uric acid versus non-uric acid kidney stones using dual-energy CT. Acad Radiol. 2007;14:1441–1447. [PubMed: 18035274]
140. Marin D, Davis D, Roy Choudhury K, et al. Characterization of small focal renal lesions: diagnostic accuracy with single-phase contrast-enhanced dual-energy CT with material attenuation analysis compared with conventional attenuation measurements. Radiology. 2017;284:737–747. [PubMed: 28353408]
141. Manoharan D, Sharma S, Das CJ, Kumar R, Singh G, Kumar P. Single-acquisition triple-bolus dual-energy CT protocol for comprehensive evaluation of renal masses: a single-center randomized noninferiority trial. AJR Am J Roentgenol. 2018;211:W22–W32. [PubMed: 29792728]
142. Mileto A, Nelson RC, Paulson EK, Marin D. Dual-energy MDCT for imaging the renal mass. AJR Am J Roentgenol. 2015;204:W640–W647. [PubMed: 25730444]
143. Ascenti G, Mazziotti S, Mileto A, et al. Dual-source dual-energy CT evaluation of complex cystic renal masses. AJR Am J Roentgenol. 2012;199:1026–1034. [PubMed: 23096175]
144. Mileto A, Sofue K, Marin D. Imaging the renal lesion with dual-energy multidetector CT and multi-energy applications in clinical practice: what can it truly do for you? Eur Radiol. 2016;26:3677–3690. [PubMed: 26801162]
145. Jung DC, Oh YT, Kim MD, Park M. Usefulness of the virtual monochromatic image in dual-energy spectral CT for decreasing renal cyst pseudoenhancement: a phantom study. AJR Am J Roentgenol. 2012;199:1316–1319. [PubMed: 23169724]
146. Mileto A, Nelson RC, Samei E, et al. Impact of dual-energy multi-detector row CT with virtual monochromatic imaging on renal cyst pseudoenhancement: in vitro and in vivo study. Radiology. 2014;272:767–776. [PubMed: 24844472]
147. Mileto A, Allen BC, Pietryga JA, et al. Characterization of incidental renal mass with dual-energy CT: diagnostic accuracy of effective atomic number maps for discriminating nonenhancing cysts from enhancing masses. AJR Am J Roentgenol. 2017;209:W221–W230. [PubMed: 28705069]
148. Mileto A, Marin D, Alfaro-Cordoba M, et al. Iodine quantification to distinguish clear cell from papillary renal cell carcinoma at dual-energy multidetector CT: a multireader diagnostic performance study. Radiology. 2014;273:813–820. [PubMed: 25162309]
149. Zarzour JG, Milner D, Valentin R, et al. Quantitative iodine content threshold for discrimination of renal cell carcinomas using rapid kV-switching dual-energy CT. Abdom Radiol (NY). 2017;42:727–734. [PubMed: 27847998]
150. Dai C, Cao Y, Jia Y, et al. Differentiation of renal cell carcinoma subtypes with different iodine quantification methods using single-phase contrast-enhanced dual-energy CT: areal vs. volumetric analyses. Abdom Radiol (NY). 2018;43:672–678. [PubMed: 28721478]
151. Wan Y, Guo H, Ji L, Li Z, Gao J. Gemstone spectral imaging dual-energy computed tomography for differentiation of renal cell carcinoma and minimal-fat renal angiomyolipoma. J Cancer Res Ther. 2018;14: S394–S399. [PubMed: 29970695]
152. Kijewski PK, Bjarngard BE. The use of computed tomography data for radiotherapy dose calculations. Int J Radiat Oncol Biol Phys. 1978;4:429–435. [PubMed: 99398]

153. Parker RP, Hobday PA, Cassell KJ. The direct use of CT numbers in radiotherapy dosage calculations for inhomogeneous media. Phys Med Biol. 1979;24:802–809. [PubMed: 472014]
154. Constantinou C, Harrington JC, DeWerd LA. An electron density calibration phantom for CT-based treatment planning computers. Med Phys. 1992;19:325–327. [PubMed: 1584125]
155. Mustafa AA, Jackson DF. The relation between x-ray CT numbers and charged particle stopping powers and its significance for radiotherapy treatment planning. Phys Med Biol. 1983;28:169. [PubMed: 6408654]
156. White DR, Booz J, Griffith RV, Spokas JJ, Wilson IJ. Tissue Substitutes in Radiation Dosimetry and. Measurement; 1989;1473–6691.
157. Schneider U, Pedroni E, Lomax A. The calibration of CT Hounsfield units for radiotherapy treatment planning. Phys Med Biol. 1996;41:111. [PubMed: 8685250]
158. Nakao M, Ozawa S, Yamada K, et al. Tolerance levels of CT number to electron density table for photon beam in radiotherapy treatment planning system. J Appl Clin Med Phys. 2018;19:271–275.
159. Kilby W, Sage J, Rabett V. Tolerance levels for quality assurance of electron density values generated from CT in radiotherapy treatment planning. Phys Med Biol. 2002;47:1485–1492. [PubMed: 12043814]
160. Thomas SJ. Relative electron density calibration of CT scanners for radiotherapy treatment planning. Br J Radiol. 1999;72:781–786. [PubMed: 10624344]
161. Frank V, Slobodan D. Sensitivity study for CT image use in Monte Carlo treatment planning. Phys Med Biol. 2005;50:937. [PubMed: 15798266]
162. Wilfried S, Thomas B, Wolfgang S. Correlation between CT numbers and tissue parameters needed for Monte Carlo simulations of clinical dose distributions. Phys Med Biol. 2000;45:459. [PubMed: 10701515]
163. Jiang H, Seco J, Paganetti H. Effects of Hounsfield number conversion on CT based proton Monte Carlo dose calculations. Med Phys. 2007;34:1439–1449. [PubMed: 17500475]
164. Kanematsu N, Inaniwa T, Nakao M. Modeling of body tissues for Monte Carlo simulation of radiotherapy treatments planned with conventional x-ray CT systems. Phys Med Biol. 2016;61:5037–5050. [PubMed: 27300449]
165. Landry G, Reniers B, Murrer L, et al. Sensitivity of low energy brachytherapy Monte Carlo dose calculations to uncertainties in human tissue composition. Med Phys. 2010;37:5188–5198. [PubMed: 21089752]
166. Zhu J, Penfold SN. Dosimetric comparison of stopping power calibration with dual-energy CT and single-energy CT in proton therapy treatment planning. Med Phys. 2016;43:2845–2854. [PubMed: 27277033]
167. Peeler CR, Mirkovic D, Titt U, et al. Clinical evidence of variable proton biological effectiveness in pediatric patients treated for ependymoma. Radiother Oncol. 2016;121:395–401. [PubMed: 27863964]
168. Newpower M, Patel D, Bronk L, et al. Using the proton energy spectrum and microdosimetry to model proton relative biological effectiveness. Int J Radiat Oncol Biol Phys. 2019;104:316–324. [PubMed: 30731186]
169. Saito M, Sagara S. Simplified derivation of stopping power ratio in the human body from dual-energy CT data. Med Phys. 2017;44:4179–4187. [PubMed: 28556239]
170. Bourque AE, Carrier JF, Bouchard H. A stoichiometric calibration method for dual energy computed tomography. Phys Med Biol. 2014;59:2059–2088. [PubMed: 24694786]
171. Taasti VT, Michalak GJ, Hansen DC, et al. Validation of proton stopping power ratio estimation based on dual energy CT using fresh tissue samples. Phys Med Biol. 2017;63:015012. [PubMed: 29057753]
172. Xie Y, Ainsley C, Yin L, et al. Ex vivo validation of a stoichiometric dual energy CT proton stopping power ratio calibration. Phys Med Biol. 2018;63:055016. [PubMed: 29513647]
173. Zhang S, Han D, Politte DG, Williamson JF, O'Sullivan JA. Impact of joint statistical dual-energy CT reconstruction of proton stopping power images: Comparison to image- and sinogram-domain material decomposition approaches. Med Phys. 2018;45:2129–2142. [PubMed: 29570809]

174. Wohlfahrt P, Möhler C, Richter C, Greilich S. Evaluation of stopping-power prediction by dual- and single-energy computed tomography in an anthropomorphic ground-truth phantom. Int J Radiat Oncol Biol Phys. 2018;100:244–253. [PubMed: 29079119]

175. Hünemohr N, Krauss B, Tremmel C, Ackermann B, Jäkel O, Greilich S. Experimental verification of ion stopping power prediction from dual energy CT data in tissue surrogates. Phys Med Biol. 2014;59:83–96. [PubMed: 24334601]

176. Möhler C, Wohlfahrt P, Richter C, Greilich S. Range prediction for tissue mixtures based on dual-energy CT. Phys Med Biol. 2016;61:N268–N275. [PubMed: 27182757]

177. Hudobivnik N, Schwarz F, Johnson T, et al. Comparison of proton therapy treatment planning for head tumors with a pencil beam algorithm on dual and single energy CT images. Med Phys. 2016;43:495. [PubMed: 26745942]

178. Bar E, Lalonde A, Zhang R, et al. Experimental validation of two dual-energy CT methods for proton therapy using heterogeneous tissue samples. Med Phys. 2018;45:48–59. [PubMed: 29134674]

179. Hunemohr N, Krauss B, Dinkel J, et al. Ion range estimation by using dual energy computed tomography. Z Med Phys. 2013;23:300–313. [PubMed: 23597413]

180. Landry G, Parodi K, Wildberger JE, Verhaegen F. Deriving concentrations of oxygen and carbon in human tissues using single- and dual-energy CT for ion therapy applications. Phys Med Biol. 2013;58:5029–5048. [PubMed: 23831541]

181. Landry G, Reniers B, Granton PV, et al. Extracting atomic numbers and electron densities from a dual source dual energy CT scanner: experiments and a simulation model. Radiother Oncol. 2011;100:375–379. [PubMed: 21924780]

182. Bazalova M, Carrier J-F, Beaulieu L, Verhaegen F. Tissue segmentation in Monte Carlo treatment planning: a simulation study using dual-energy CT images. Radiother Oncol. 2008;86:93–98. [PubMed: 18068841]

183. Landry G, Gaudreault M, van Elmpt W, Wildberger JE, Verhaegen F. Improved dose calculation accuracy for low energy brachytherapy by optimizing dual energy CT imaging protocols for noise reduction using sinogram affirmed iterative reconstruction. Z Med Phys. 2016; 26:75–87. [PubMed: 26422576]

184. Huang JY, Kerns JR, Nute JL, et al. An evaluation of three commercially available metal artifact reduction methods for CT imaging. Phys Med Biol. 2015;60:1047–1067. [PubMed: 25585685]

185. Cote N, Bedwani S, Carrier JF. Improved tissue assignment using dual-energy computed tomography in low-dose rate prostate brachytherapy for Monte Carlo dose calculation. Med Phys. 2016;43:2611. [PubMed: 27147370]

186. Malusek A, Magnusson M, Sandborg M, Alm CG. A model-based iterative reconstruction algorithm DIRA using patient-specific tissue classification via DECT for improved quantitative CT in dose planning. Med Phys. 2017;44:2345–2357. [PubMed: 28369941]

187. Mashouf S, Lechtman E, Lai P, et al. Dose heterogeneity correction for low-energy brachytherapy sources using dual-energy CT images. Phys Med Biol. 2014;59:5305–5316. [PubMed: 25146446]

188. Remy C, Lalonde A, Beliveau-Nadeau D, Carrier JF, Bouchard H. Dosimetric impact of dual-energy CT tissue segmentation for low-energy prostate brachytherapy: a Monte Carlo study. Phys Med Biol. 2018;63:025013. [PubMed: 29260727]

189. Fave X, Zhang L, Yang J, et al. Delta-radiomics features for the prediction of patient outcomes in non-small cell lung cancer. Sci Rep. 2017;7:588. [PubMed: 28373718]

190. Haralick RM, Shanmugam K. Textural features for image classification. IEEE Trans Syst Man Cybernet. 1973;6:610–621.

191. Galloway MM. Texture analysis using gray level run lengths. Comput Graph Image Process. 1975;4:172–179.

192. Tang X. Texture information in run-length matrices. IEEE Trans Image Process. 1998;7:1602–1609. [PubMed: 18276225]

193. Amadasun M, King R. Textural features corresponding to textural properties. IEEE Trans Syst Man Cybern. 1989;19:1264–1274.

194. Thibault G, Fertil B, Navarro C, et al. Shape and texture indexes application to cell nuclei classification. Int J Pattern Recognit Artif Intell. 2013;27:1357002.
195. Solomon J, Mileto A, Nelson RC, Roy Choudhury K, Samei E. Quantitative features of liver lesions, lung nodules, and renal stones at multi-detector row CT examinations: dependency on radiation dose and reconstruction algorithm. Radiology. 2016;279:185–194. [PubMed: 26624973]
196. Larue R, van Timmeren JE, de Jong EEC, et al. Influence of gray level discretization on radiomic feature stability for different CT scanners, tube currents and slice thicknesses: a comprehensive phantom study. Acta Oncol. 2017;56:1544–1553. [PubMed: 28885084]
197. Ger RB, Zhou S, Chi P-CM, et al. Comprehensive investigation on controlling for CT imaging variabilities in radiomics studies. Sci Rep. 2018;8;13047. [PubMed: 30158540]
198. Court L, Fave X, Mackin D, Lee J, Yang J, Zhang L. Computational resources for radiomics. Transl Cancer Res. 2016;5:340–348.
199. Zwanenburg A, Leger S, Vallières M, Löck S. Image biomarker standardisation initiative. arXiv preprint arXiv:161207003; 2016.
200. Foy JJ, Robinson KR, Li H, Giger ML, Al-Hallaq H, Armato SG 3rd. Variation in algorithm implementation across radiomics software. J Med Imaging (Bellingham). 2018;5:044505. [PubMed: 30840747]
201. Chalkidou A, O'Doherty MJ, Marsden PK. False discovery rates in PET and CT studies with texture features: a systematic review. PLoS One. 2015;10:e0124165. [PubMed: 25938522]
202. Larue RT, Defraene G, De Ruysscher D, Lambin P, Van Elmpt W. Quantitative radiomics studies for tissue characterization: a review of technology and methodological procedures. Br J Radiol. 2017;90:20160665. [PubMed: 27936886]
203. Thawani R, McLane M, Beig N, et al. Radiomics and radiogenomics in lung cancer: a review for the clinician. Lung Cancer. 2017;115:34–41. [PubMed: 29290259]
204. Chakraborty J, Midya A, Gazit L et al. CT radiomics to predict high-risk intraductal papillary mucinous neoplasms of the pancreas. Med Phys. 2018;45:5019–5029. [PubMed: 30176047]
205. Shikhaliev PM. Soft tissue imaging with photon counting spectroscopic CT. Phys Med Biol. 2015;60:2453–2474. [PubMed: 25739788]
206. Boussel L, Coulon P, Thran A, et al. Photon counting spectral CT component analysis of coronary artery atherosclerotic plaque samples. Br J Radiol. 2014;87:20130798. [PubMed: 24874766]
207. Kirkbride TE, Raja AY, Muller K, Bateman CJ, Becce F, Anderson NG. Discrimination between calcium hydroxyapatite and calcium oxalate using multienergy spectral photon-counting CT. AJR Am J Roentgenol. 2017;209:1088–1092. [PubMed: 28834448]
208. Gutjahr R, Polster C, Henning A, et al. Dual energy CT kidney stone differentiation in photon counting computed tomography. Proc SPIE Int Soc Opt Eng. 2017;10132:1013237. [PubMed: 28943700]
209. Ferrero A, Gutjahr R, Henning A, et al. Renal stone characterization using high resolution imaging mode on a photon counting detector CT system. Proc SPIE Int Soc Opt Eng. 2017;10132:1013237. [PubMed: 28943700]
210. McCollough CH, Leng S, Yu L, Fletcher JG. Dual- and multi-energy CT: principles, technical approaches, and clinical applications. Radiology. 2015;276:637–653. [PubMed: 26302388]
211. Mannil M, Hickethier T, von Spiczak J, et al. Photon-counting CT: high-resolution imaging of coronary stents. Invest Radiol. 2018;53:143–149. [PubMed: 28945655]
212. Zhou W, Lane JI, Carlson ML, et al. Comparison of a photon-counting-detector CT with an energy-integrating-detector CT for temporal bone imaging: a cadaveric study. AJNR Am J Neuroradiol. 2018;39:1733–1738. [PubMed: 30093479]
213. Willemink MJ, Persson M, Pourmorteza A, Pelc NJ, Fleischmann D. Photon-counting CT: technical principles and clinical prospects. Radiology. 2018;289:293–312. [PubMed: 30179101]
214. Leng S, Yu Z, Halaweish A, et al. Dose-efficient ultrahigh-resolution scan mode using a photon counting detector computed tomography system. J Med Imaging (Bellingham). 2016;3:043504. [PubMed: 28042589]

215. Chen H, Xu C, Persson M, Danielsson M. Optimization of beam quality for photon-counting spectral computed tomography in head imaging: simulation study. J Med Imaging (Bellingham). 2015;2:043504. [PubMed: 26835495]

216. Li Z, Leng S, Yu Z, Kappler S, McCollough CH. Estimation of signal and noise for a whole-body research photon-counting CT system. J Med Imaging (Bellingham). 2017;4:023505. [PubMed: 28653013]

217. Symons R, Reich DS, Bagheri M, et al. Photon-counting computed tomography for vascular imaging of the head and neck: first in vivo human results. Invest Radiol. 2018;53:135–142. [PubMed: 28926370]

218. Zhou W, Bartlett DJ, Diehn FE, et al. Reduction of metal artifacts and improvement in dose efficiency using photon-counting detector computed tomography and tin filtration. Invest Radiol. 2019;54:204–211. [PubMed: 30562270]

219. Cropp RJ, Seslija P, Tso D, Thakur Y. Scanner and kVp dependence of measured CT numbers in the ACR CT phantom. J Appl Clin Med Phys. 2013;14:338–349.

220. Szczykutowicz TP, DuPlissis A, Pickhardt PJ. Variation in CT number and image noise uniformity according to patient positioning in MDCT. AJR Am J Roentgenol. 2017;208:1064–1072. [PubMed: 28267350]

221. Michalak G, Grimes J, Fletcher J, et al. Technical note: improved CT number stability across patient size using dual-energy CT virtual monoenergetic imaging. Med Phys. 2016;43:513–517. [PubMed: 26745944]

222. Cheung JP, Shugard E, Mistry N, Pouliot J, Chen J. Evaluating the impact of extended field-of-view CT reconstructions on CT values and dosimetric accuracy for radiation therapy. Med Phys. 2019;46:892–901. [PubMed: 30457170]

223. Cruz-Bastida JP, Gomez-Cardona D, Li K, et al. Hi-Res scan mode in clinical MDCT systems: experimental assessment of spatial resolution performance. Med Phys. 2016;43:2399–2409. [PubMed: 27147351]

224. Marsh RM, Silosky MS. The effects of patient positioning when interpreting CT dose metrics: a phantom study. Med Phys. 2017;44: 1514–1524. [PubMed: 28133763]

225. Kaasalainen T, Palmu K, Reijonen V, Kortesniemi M. Effect of patient centering on patient dose and image noise in chest CT. AJR Am J Roentgenol. 2014;203:123–130. [PubMed: 24951205]

226. Saltybaeva N, Schmidt B, Wimmer A, Flohr T, Alkadhi H. Precise and automatic patient positioning in computed tomography: avatar modeling of the patient surface using a 3-dimensional camera. Invest Radiol. 2018;53:641–646. [PubMed: 29762259]

227. Booij R, Budde RPJ, Dijkshoorn ML, van Straten M. Accuracy of automated patient positioning in CT using a 3D camera for body contour detection. Eur Radiol. 2019;29:2079–2088. [PubMed: 30306328]

228. Liu X, Yu L, Primak AN, McCollough CH. Quantitative imaging of element composition and mass fraction using dual-energy CT: three-material decomposition. Med Phys. 2009;36:1602–1609. [PubMed: 19544776]

229. Xue Y, Ruan R, Hu X, et al. Statistical image-domain multimaterial decomposition for dual-energy CT. Med Phys. 2017;44:886–901. [PubMed: 28060999]

230. Long Y, Fessler JA. Multi-material decomposition using statistical image reconstruction for spectral CT. IEEE Trans Med Imaging. 2014;33:1614–1626. [PubMed: 24801550]

231. Winklhofer S, Lambert JW, Sun Y, Wang ZJ, Sun DS, Yeh BM. Pelvic beam-hardening artifacts in dual-energy CT image reconstructions: occurrence and impact on image quality. AJR Am J Roentgenol. 2016;208:114–123. [PubMed: 27786561]

232. Chen B, Zhang Z, Xia D, Sidky EY, Pan X. Algorithm-enabled partial-angular-scan configurations for dual-energy CT. Med Phys. 2018;45:1857–1870. [PubMed: 29516523]

233. Tao S, Rajendran K, McCollough CH, Leng S. Material decomposition with prior knowledge aware iterative denoising (MD-PKAID). Phys Med Biol. 2018;63:195003. [PubMed: 30136655]

234. Su KH, Kuo JW, Jordan DW, et al. Machine learning-based dual-energy CT parametric mapping. Phys Med Biol. 2018;63:125001. [PubMed: 29787382]

235. McCollough CH, Boedeker K, Cody D, et al. Principles and applications of multi-energy CT report of AAPM Task Group 291. Med Phys. Epub ahead of print.

236. Taguchi K, Stierstorfer K, Polster C, Lee O, Kappler S. Spatio-energetic cross-talk in photon counting detectors: numerical detector model (PcTK) and workflow for CT image quality assessment. Med Phys. 2018;45:1985–1998. [PubMed: 29537627]

237. Hsieh SS, Rajbhandary PL, Pelc NJ. Spectral resolution and high-flux capability tradeoffs in CdTe detectors for clinical CT. Med Phys. 2018;45:1433–1443. [PubMed: 29418004]

238. Zimmerman KC, Schmidt TG. Experimental comparison of empirical material decomposition methods for spectral CT. Phys Med Biol. 2015;60:3175–3191. [PubMed: 25813054]

239. Schmidt TG. CT energy weighting in the presence of scatter and limited energy resolution. Med Phys. 2010;37:1056–1067. [PubMed: 20384241]

240. Schmidt TG, Barber RF, Sidky EY. A spectral CT method to directly estimate basis material maps from experimental photon-counting data. IEEE Trans Med Imaging. 2017;36:1808–1819. [PubMed: 28436858]

241. Xu C, Danielsson M, Karlsson S, Svensson C, Bornefalk H. Preliminary evaluation of a silicon strip detector for photon-counting spectral CT. Nucl Instrum Methods Phys Res Sect A. 2012;677:45–51.

242. Iwanczyk JS, Nygard E, Meirav O, et al. Photon counting energy dispersive detector arrays for x-ray imaging. IEEE Trans Nucl Sci. 2009;56:535–542. [PubMed: 19920884]

243. Szczykutowicz TP, Mistretta CA. Experimental realization of fluence field modulated CT using digital beam attenuation. Phys Med Biol. 2014;59:1305–1326. [PubMed: 24556823]

244. Shunhavanich P, Hsieh SS, Pelc NJ. Fluid-filled dynamic bowtie filter: Description and comparison with other modulators. Med Phys. 2019;46:127–139. [PubMed: 30383310]

245. Schmidt TG, Barber RF, Sidky EY. A spectral CT method to directly estimate basis material maps from experimental photon-counting Data. IEEE Trans Med Imaging. 2017;36:1808–1819. [PubMed: 28436858]

246. Yu Z, Leng S, Li Z, McCollough CH. Spectral prior image constrained compressed sensing (spectral PICCS) for photon-counting computed tomography. Phys Med Biol. 2016;61:6707–6732. [PubMed: 27551878]

247. Park S-J, Kang D-Y, Sohn K-H, et al. Immediate mild reactions to CT with iodinated contrast media: strategy of contrast media readministration without corticosteroids. Radiology. 2018;288:710–716. [PubMed: 29786483]

248. Kim TH, Yoon SH, Lee SY, et al. Biphasic and protracted anaphylaxis to iodinated contrast media. Eur Radiol. 2018;28:1242–1252. [PubMed: 28956131]

249. ACR Committee on Drugs and Contrast Media. ACR Manual on Contrast Media v. 11; 2020. https://www.acr.org/Clinical-Resources/Contrast-Manual. Accessed February 14, 2020.

250. Cochran ST, Bomyea K, Sayre JW. Trends in adverse events after IV administration of contrast media. AJR Am J Roentgenol. 2001;176: 1385–1388. [PubMed: 11373197]

251. Mortelé KJ, Oliva M-R, Ondategui S, Ros PR, Silverman SG. Universal use of nonionic iodinated contrast medium for CT: evaluation of safety in a large urban teaching hospital. AJR Am J Roentgenol. 2005;184:31–34. [PubMed: 15615946]

252. Wang CL, Cohan RH, Ellis JH, Caoili EM, Wang G, Francis IR. Frequency, outcome, and appropriateness of treatment of nonionic iodinated contrast media reactions. AJR Am J Roentgenol. 2008;191:409–415. [PubMed: 18647910]

253. Kielar AZ, Patlas MN, Katz DS. Oral contrast for CT in patients with acute non-traumatic abdominal and pelvic pain: what should be its current role? Emerg Radiol. 2016;23:477–481. [PubMed: 27166963]

254. Megibow AJ, Bosniak MA. Dilute barium as a contrast agent for abdominal CT. AJR Am J Roentgenol. 1980;134:1273–1274. [PubMed: 6770647]

255. Kong X, Sheng HX, Lu GM, et al. Xenon-enhanced dual-energy CT lung ventilation imaging: techniques and clinical applications. AJR Am J Roentgenol. 2014;202:309–317. [PubMed: 24450670]

256. Pistoia F, Johnson DW, Darby JM, Horton JA, Applegate LJ, Yonas H. The role of xenon CT measurements of cerebral blood flow in the clinical determination of brain death. Am J Neuroradiol. 1991;12:97. [PubMed: 1899528]

257. Sase S, Yamamoto H, Kawashima E, Tan X, Sawa Y. Discrimination between patients with alzheimer disease and healthy subjects using layer analysis of cerebral blood flow and xenon solubility coefficient in xenon-enhanced computed tomography. J Comput Assist Tomogr. 2017;41:477–483. [PubMed: 28505626]

258. Lambert JW, Sun Y, Gould RG, Ohliger MA, Li Z, Yeh BM. An image-domain contrast material extraction method for dual-energy computed tomography. Invest Radiol. 2017;52:245–254. [PubMed: 27875338]

259. Lambert JW, Sun Y, Ordovas KG, Gould RG, Wang S, Yeh BM. Improved calcium scoring at dual-energy computed tomography angiography using a high-z contrast element and novel material separation technique. J Comput Assist Tomogr. 2018;42:459–466. [PubMed: 28937491]

260. X-ray Transition Energies Database (Version 1.2) National Institute of Standards and Technology; 2005. http://physics.nist.gov/XrayTrans. Accessed May 05, 2019.

261. Riederer SJ, Mistretta CA. Selective iodine imaging using K-edge energies in computerized x-ray tomography. Med Phys. 1977;4:474–481. [PubMed: 927384]

262. Kanda T, Nakai Y, Oba H, Toyoda K, Kitajima K, Furui S. Gadolinium deposition in the brain. Magn Reson Imaging. 2016;34:1346–1350. [PubMed: 27613998]

263. Ozturk K, Nas OF, Soylu E, Hakyemez B. Signal changes in the den-tate nucleus and globus pallidus on unenhanced T1-weighted magnetic resonance images after intrathecal administration of macrocyclic gadolinium contrast agent. Invest Radiol. 2018;53:535–540. [PubMed: 29727401]

264. FitzGerald PF, Colborn RE, Edic PM, et al. CT image contrast of high-z elements: phantom imaging studies and clinical implications. Radiology. 2016;278:723–733. [PubMed: 26356064]

265. Curtis TE, Roeder RK. Effects of calibration methods on quantitative material decomposition in photon-counting spectral computed tomography using a maximum a posteriori estimator. Med Phys. 2017;44:5187–5197. [PubMed: 28681402]

266. Sun IC, Na JH, Jeong SY, et al. Biocompatible glycol chitosan-coated gold nanoparticles for tumor-targeting CT imaging. Pharm Res. 2014;31: 1418–1425. [PubMed: 23934255]

267. Li J, Chaudhary A, Chmura SJ, et al. A novel functional CT contrast agent for molecular imaging of cancer. Phys Med Biol. 2010;55:4389–4397. [PubMed: 20647599]

268. Cole LE, Vargo-Gogola T, Roeder RK. Contrast-enhanced X-ray detection of breast microcalcifications in a murine model using targeted gold nanoparticles. ACS Nano. 2014;8:7486–7496. [PubMed: 24992365]

269. Chanda N, Upendran A, Boote EJ, et al. Gold nanoparticle based X-ray contrast agent for tumor imaging in mice and dog: a potential nanoplatform for computer tomography theranostics. J Biomed Nanotechnol. 2014;10:383–392. [PubMed: 24730234]

270. Rathnayake S, Mongan J, Torres AS, et al. In vivo comparison of tantalum, tungsten, and bismuth enteric contrast agents to complement intravenous iodine for double-contrast dual-energy CT of the bowel. Contrast Media Mol Imaging. 2016;11:254–261. [PubMed: 26892945]

271. Mongan J, Rathnayake S, Fu Y, et al. In vivo differentiation of complementary contrast media at dual-energy CT. Radiology. 2012;265: 267–272. [PubMed: 22778447]

272. Zhou Z, Kong B, Yu C, et al. Tungsten oxide nanorods: an efficient nanoplatform for tumor CT imaging and photothermal therapy. Sci Rep. 2014;4:3653. [PubMed: 24413483]

273. Liu J, Han J, Kang Z, et al. In vivo near-infrared photothermal therapy and computed tomography imaging of cancer cells using novel tungsten-based theranostic probe. Nanoscale. 2014;6:5770–5776. [PubMed: 24736832]

274. Unger E, Ytterbium-DTPA GF. A potential intravascular contrast agent. Invest Radiol. 1986;21:802–807. [PubMed: 3771152]

275. Liu Z, Li Z, Liu J, et al. Long-circulating Er3+-doped Yb2O3 up-conversion nanoparticle as an in vivo X-Ray CT imaging contrast agent. Biomaterials. 2012;33:6748–6757. [PubMed: 22770569]

276. Liu Y, Liu J, Ai K, Yuan Q, Lu L. Recent advances in ytterbium-based contrast agents for in vivo X-ray computed tomography imaging: promises and prospects. Contrast Media Mol Imaging. 2014;9:26–36. [PubMed: 24470292]

277. Pan D, Schirra CO, Senpan A, et al. An early investigation of ytterbium nanocolloids for selective and quantitative “multicolor” spectral CT imaging. ACS Nano. 2012;6:3364–3370. [PubMed: 22385324]

278. FitzGerald PF, Butts MD, Roberts JC, et al. A proposed computed tomography contrast agent using carboxybetaine zwitterionic tantalum oxide nanoparticles: imaging, biological, and physicochemical performance. Invest Radiol. 2016;51:786–796. [PubMed: 27115702]

279. Torres AS, Bonitatibus PJ Jr., Colborn RE, et al. Biological performance of a size-fractionated core-shell tantalum oxide nanoparticle x-ray contrast agent. Invest Radiol. 2012;47:578–587. [PubMed: 22836312]

280. Lambert JW, Sun Y, Stillson C, et al. An intravascular tantalum oxide-based CT contrast agent: preclinical evaluation emulating overweight and obese patient size. Radiology. 2018;289:103–110. [PubMed: 29969071]

281. Xiao Q, Bu W, Ren Q, et al. Radiopaque fluorescence-transparent TaOx decorated upconversion nanophosphors for in vivo CT/MR/UCL tri-modal imaging. Biomaterials. 2012;33:7530–7539. [PubMed: 22840224]

282. Jin Y, Ma X, Zhang S, et al. A tantalum oxide-based core/shell nanoparticle for triple-modality image-guided chemo-thermal synergetic therapy of esophageal carcinoma. Cancer Lett. 2017;397: 61–71. [PubMed: 28351615]

283. Jin Y, Li Y, Ma X, et al. Encapsulating tantalum oxide into polypyrrole nanoparticles for X-ray CT/photoacoustic bimodal imaging-guided photothermal ablation of cancer. Biomaterials. 2014;35:5795–5804. [PubMed: 24746966]

284. Grant KL, Flohr TG, Krauss B, Sedlmair M, Thomas C, Schmidt B. Assessment of an advanced image-based technique to calculate virtual monoenergetic computed tomographic images from a dual-energy examination to improve contrast-to-noise ratio in examinations using iodinated contrast media. Invest Radiol. 2014;49:586–592. [PubMed: 24710203]

285. Wichmann JL, Noske EM, Kraft J, et al. Virtual monoenergetic dual-energy computed tomography: optimization of kiloelectron volt settings in head and neck cancer. Invest Radiol. 2014;49:735–741. [PubMed: 24872006]

286. Kaup M, Scholtz JE, Engler A, et al. Dual-energy computed tomography virtual monoenergetic imaging of lung cancer: assessment of optimal energy levels. J Comput Assist Tomogr. 2016;40:80–85. [PubMed: 26466115]

287. Wohlfahrt P, Mohler C, Stutzer K, Greilich S, Richter C. Dual-energy CT based proton range prediction in head and pelvic tumor patients. Radiother Oncol. 2017;125:526–533. [PubMed: 29050953]

288. Taasti VT, Hansen DC, Michalak GJ, et al. Theoretical and experimental analysis of photon counting detector CT for proton stopping power prediction. Med Phys. 2018;45:5186–5196. [PubMed: 30191573]

289. Taasti VT, Bäumer C, Dahlgren CV, et al. Inter-centre variability of CT-based stopping-power prediction in particle therapy: survey-based evaluation. Phys Imaging Radiat Oncol. 2018;6:25–30. [PubMed: 33458385]

290. Wohlfahrt P, Mohler C, Hietschold V, et al. Clinical implementation of dual-energy CT for proton treatment planning on pseudo-monoenergetic CT scans. Int J Radiat Oncol Biol Phys. 2017;97:427–434. [PubMed: 28068248]

291. Cui L, Her S, Borst GR, Bristow RG, Jaffray DA, Allen C. Radiosensitization by gold nanoparticles: Will they ever make it to the clinic? Radiother Oncol. 2017;124:344–356. [PubMed: 28784439]

292. Wan D, Chen D, Li K, et al. Gold nanoparticles as a potential cellular probe for tracking of stem cells in bone regeneration using dual-energy computed tomography. ACS Appl Mater Interfaces. 2016;8:32241–32249. [PubMed: 27933815]

293. Clark DP, Ghaghada K, Moding EJ, Kirsch DG, Badea CT. In vivo characterization of tumor vasculature using iodine and gold nanoparticles and dual energy micro-CT. Phys Med Biol. 2013;58:1683–1704. [PubMed: 23422321]

294. Moghiseh M, Lowe C, Lewis JG, et al. Spectral photon-counting molecular imaging for quantification of monoclonal antibody-conjugated gold nanoparticles targeted to lymphoma and breast cancer: an in vitro study. Contrast Media Mol Imaging. 2018;2018:2136840. [PubMed: 30662379]

295. Anselmo AC, Mitragotri S. A review of clinical translation of inorganic nanoparticles. AAPS J. 2015;17:1041–1054. [PubMed: 25956384]

296. Bonvalot S, Le Pechoux C, De Baere T, et al. First-in-human study testing a new radioenhancer using nanoparticles (NBTXR3) activated by radiation therapy in patients with locally advanced soft tissue sarcomas. Clin Cancer Res. 2017;23:908–917. [PubMed: 27998887]

297. Berger M, Bauser M, Frenzel T, et al. Hafnium-based contrast agents for x-ray computed tomography. Inorg Chem. 2017;56:5757–5761. [PubMed: 28430423]

298. Lencioni R, de Baere T, Soulen MC, Rilling WS, Geschwind JF. Lipiodol transarterial chemoembolization for hepatocellular carcinoma: a systematic review of efficacy and safety data. Hepatology. 2016;64: 106–116. [PubMed: 26765068]

299. Konno T, Maeda H, Iwai K, et al. Effect of arterial administration of high-molecular-weight anticancer agent SMANCS with lipid lympho-graphic agent on hepatoma: a preliminary report. Eur J Cancer Clin Oncol. 1983;19:1053–1065. [PubMed: 6311559]

300. Yamada R, Sato M, Kawabata M, Nakatsuka H, Nakamura K, Takashima S. Hepatic artery embolization in 120 patients with unresectable hepatoma. Radiology. 1983;148:397–401. [PubMed: 6306721]

301. Sofue K, Itoh T, Takahashi S, et al. Quantification of cisplatin using a modified 3-material decomposition algorithm at third-generation dual-source dual-energy computed tomography: an experimental study. Invest Radiol. 2018;53:673–680. [PubMed: 29912043]

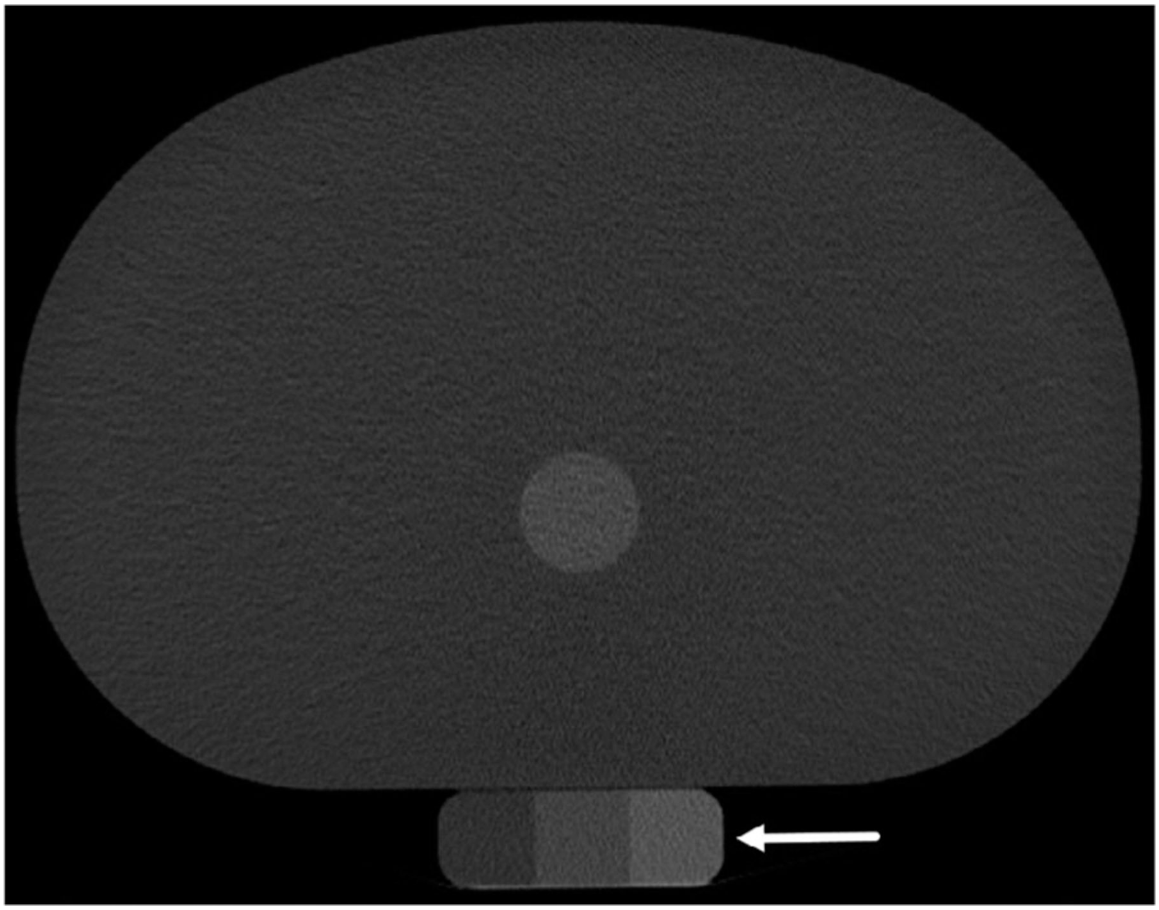

FIG. 1.
Example of synchronous scanning of a bone mineral density calibration phantom (white arrow) as it would be positioned under a patient

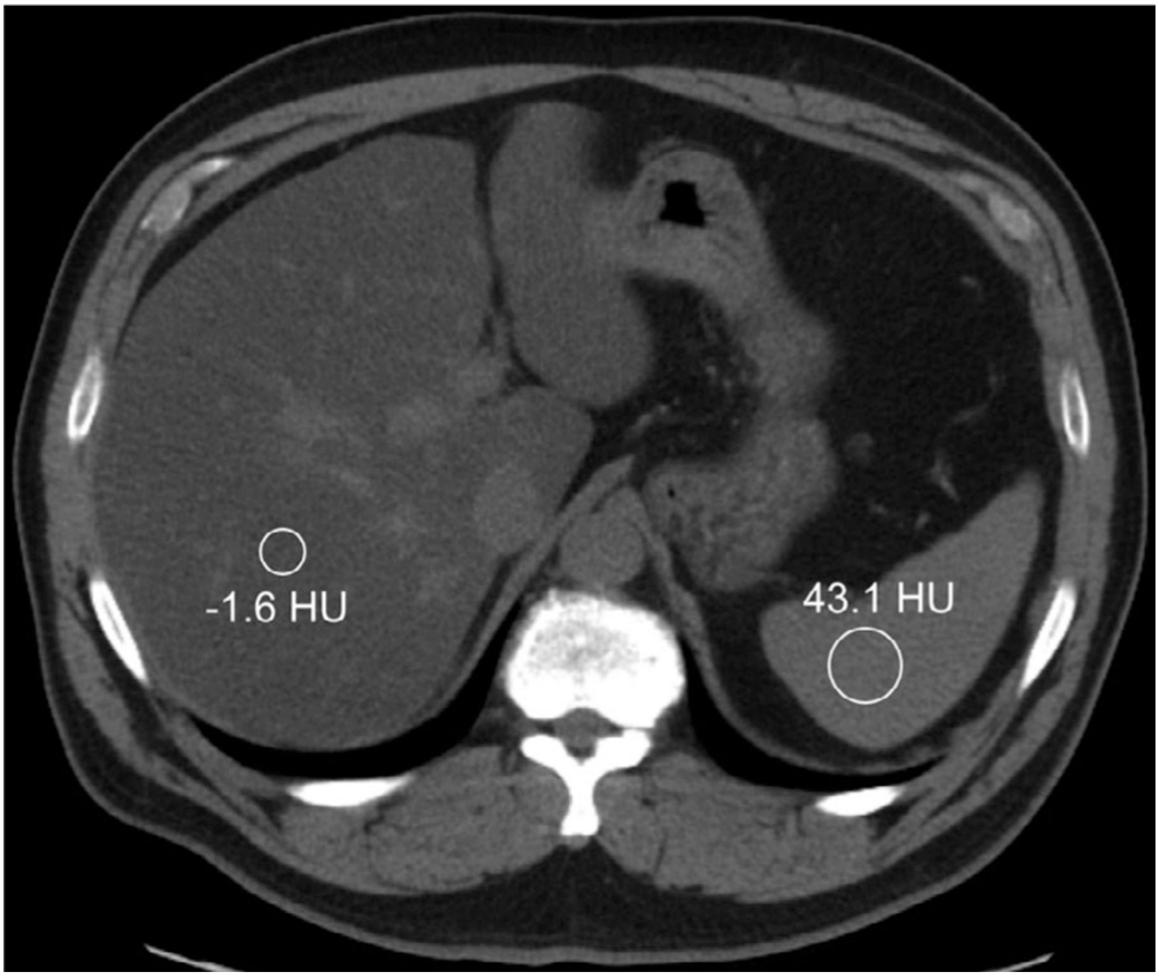

FIG. 2.
Single-energy computed tomography methodology for diagnosis of hepatic steatosis utilizes regions of interest in the liver and spleen, shown here in a 61-yr-old male seen for restaging of a pancreatic neuroendocrine tumor. The liver attenuation in this case is both below 40 HU and more than 10 HU lower than that of the spleen, indicating the presence of diffuse fat within the liver tissue.

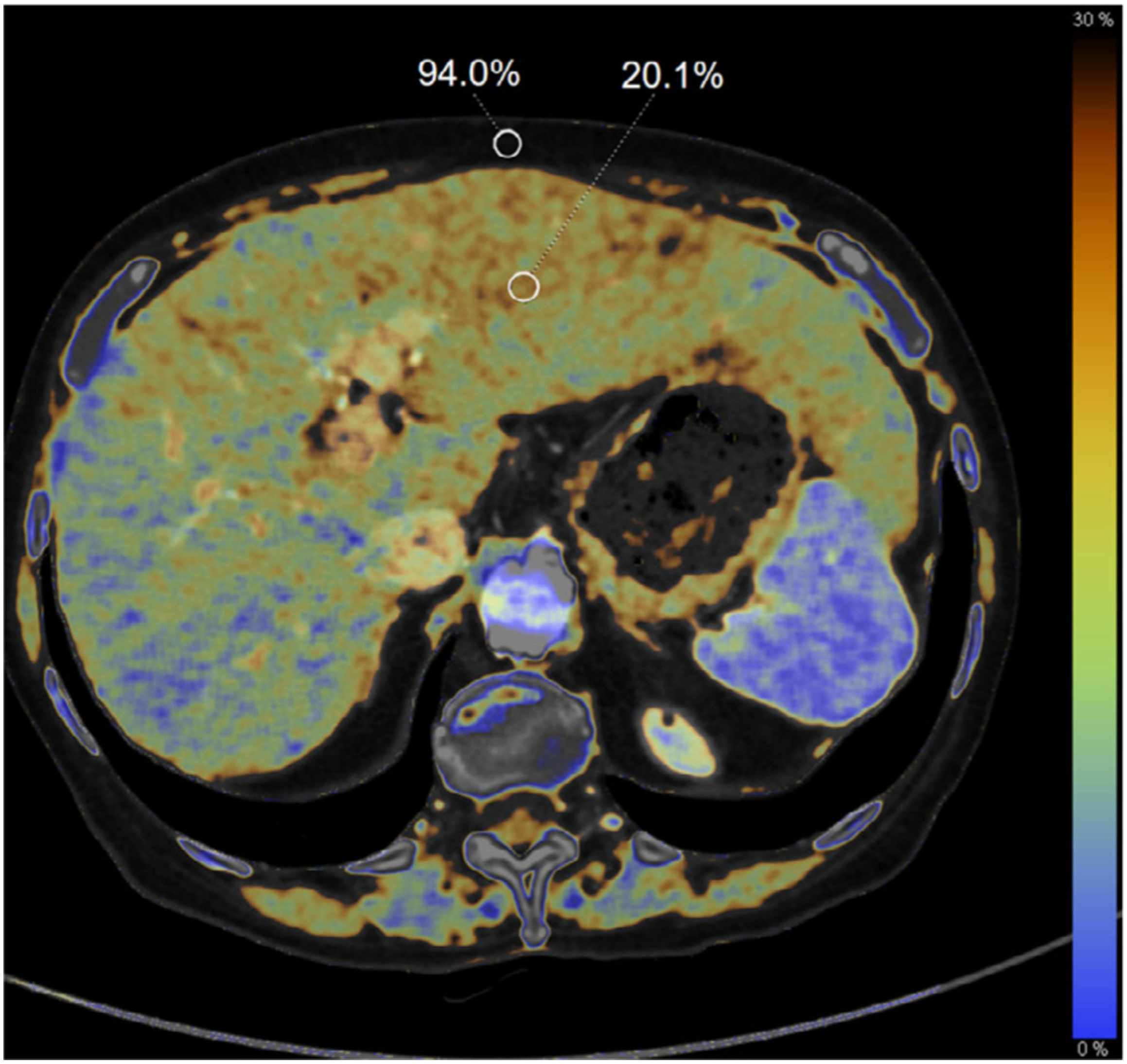

FIG. 3.

Fatty infiltration of the liver demonstrated on a dual-energy computed tomography fat map in a 75-yr-old woman with pancreatic adenocarcinoma following chemotherapy. The calculated fat fraction for regions of interest in the liver (20.1%) and subcutaneous fat (94.0%) are shown as a percent volume.

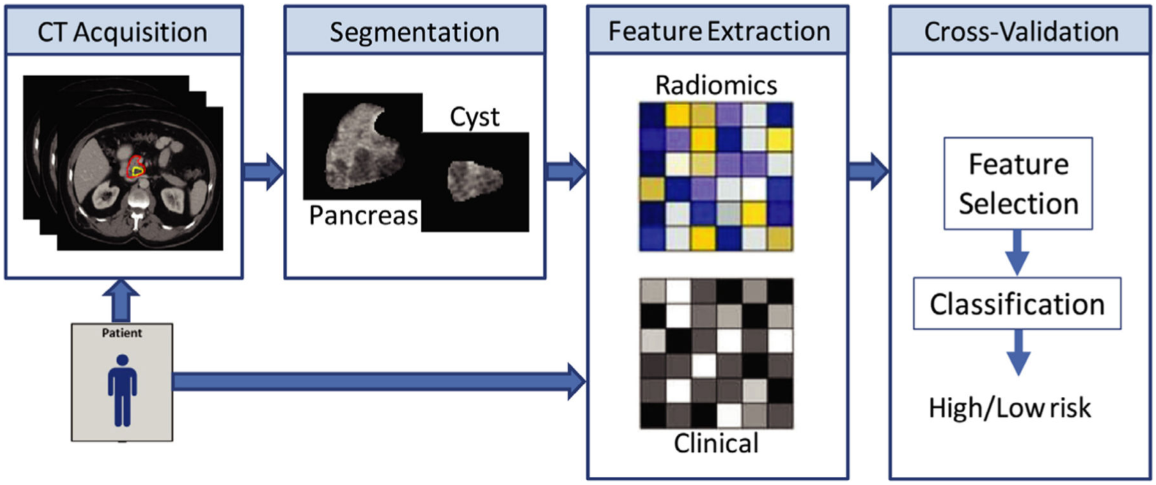

FIG. 4.

General workflow for development of radiomics-based prediction models. Patients are imaged, and the volume of interest is segmented either manually or automatically. Quantitative radiomics features are extracted from the volume and used along with other clinical or genomics data to develop a statistical model for decision support. Figure reproduced from reference.[204]

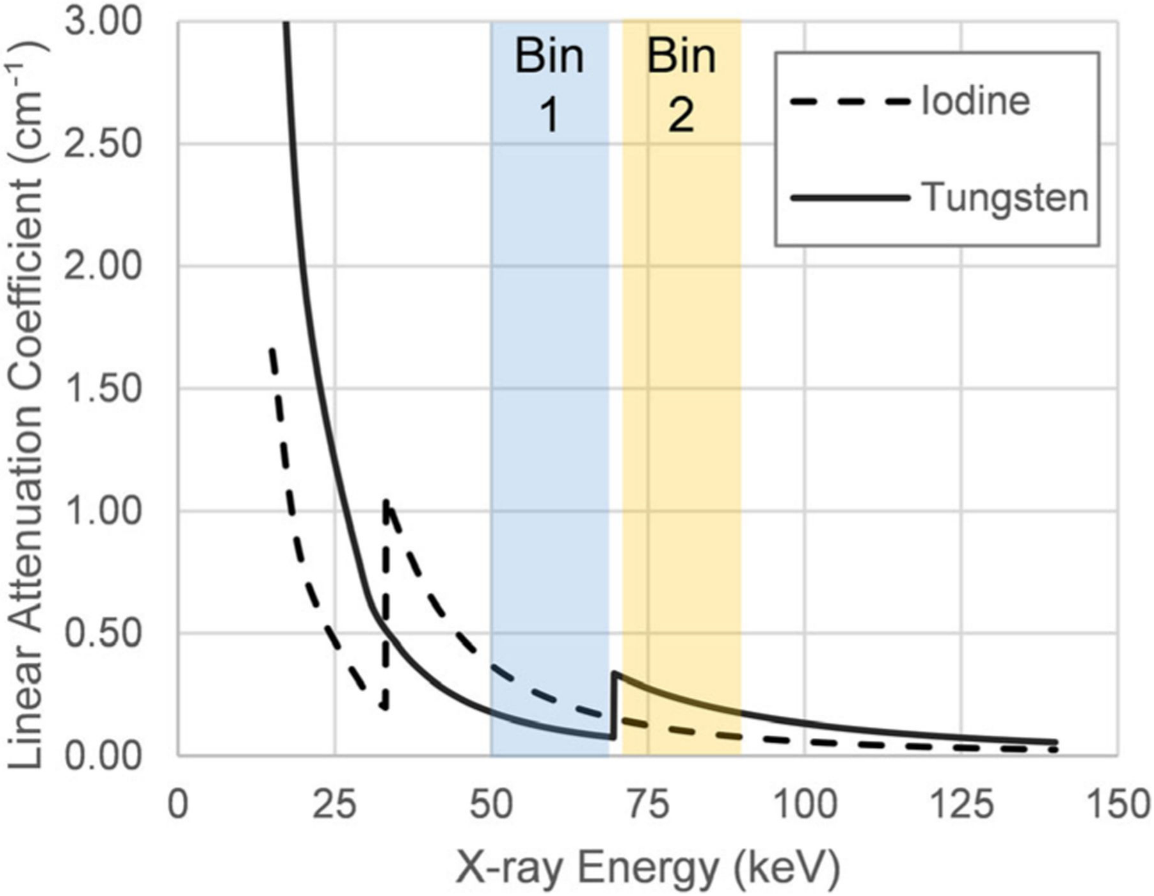

FIG. 5.

K-edges for iodine (33.2 keV) and tungsten (69.5 keV) allow for K-edge imaging. In energy bin 1 (blue), positioned just below the tungsten K-edge, iodine signal dominates, while in bin 2 (yellow), tungsten signal will be the primary contributor to contrast.

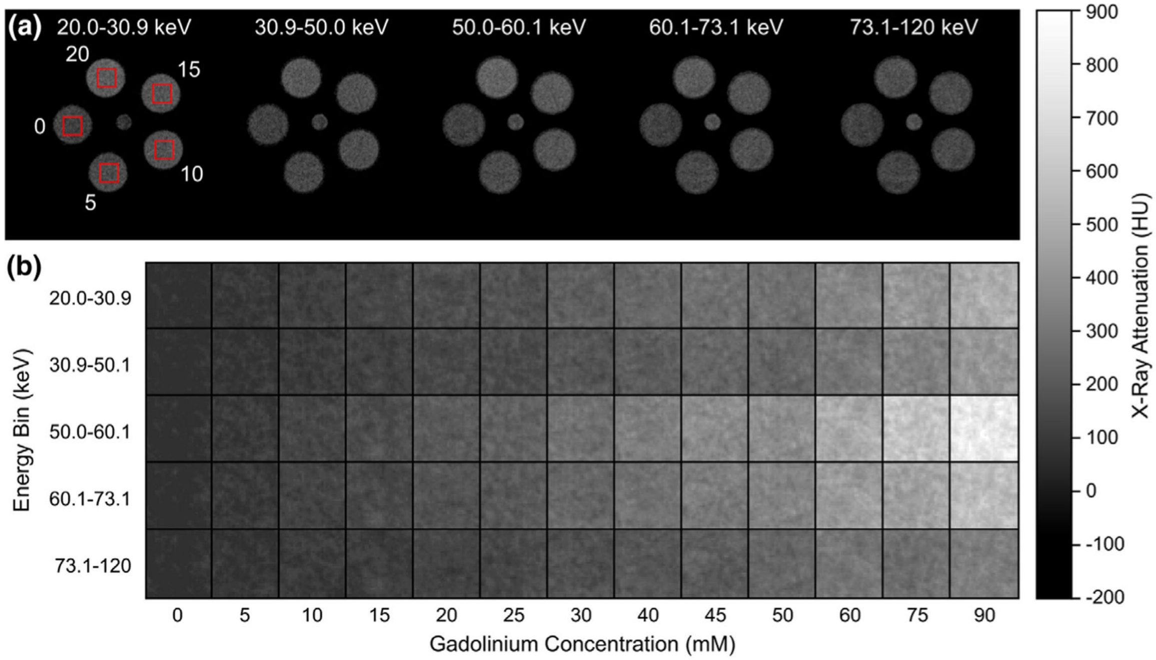

FIG. 6.

Representative (a) grayscale computed tomography image slices of a calibration phantom comprising of 0, 5, 10, 15, and 20 mM gadolinium concentrations showing example VOIs (boxes), and (b) cropped grayscale images of VOIs spanning the full range of gadolinium concentrations, for each energy bin of the photon-counting detector, demonstrating the increased attenuation of gadolinium in energy bins greater than the K-edge (50.2 keV). Note that all grayscale intensities were converted to HU. Figure reproduced from Curtis et al.[265]

Table I.

Common dual-energy CT material decomposition schemes and their application.

DECT material decomposition[a]	Applications	Anatomical region	Relevant pathologies
Iodine/water or Soft tissue[b]	Virtual removal of iodinated contrast	Head and neck, thoracic, abdominal, pelvic	Renal cell carcinoma, pulmonary function, pulmonary embolism, contrast extravasation vs hemorrhage, tumor characterization and staging
Iodine/water or soft tissue/adipose	Virtual removal of iodinated contrast in liver, fat quantification	Abdominal (liver)	Fatty liver disease, hepatocellular carcinoma, liver metastasis
Calcium/water or soft tissue	Virtual calcium/bone removal, calcium quantification	Musculoskeletal, cardiovascular, abdominal, Head and neck	Bone marrow edema, vascular plaque, renal stones, calcification and hemorrhage differentiation
Calcium/hemorrhage/brain	Brain hemorrhage evaluation	Head and neck	Differentiate intracranial hemorrhage and calcification
Uric acid	Renal stone composition gout	Abdominal extremity	Differentiate calcific and uric acid-based renal stones and gout crystais in non-contrast CT exams

[a] Applications may not be commercially available from all vendors.

[b] The use of water or soft tissue is vendor-specific.

Table II.

Spinal quantitative computed tomography bone mineral density (BMD) criteria for degenerative diseases. Table adapted from the American College of Radiology guidelines for performance of musculoskeletal quantitative computed tomography.[74]

Trabecular spine BMD range	World Health Organization diagnostic category
>120 mg/cm^3	Normal
80–120 mg/cm^3	Osteopenia
<80 mg/cm^3	Osteoporosis

Table III.

K-edge energies for current and experimental computed tomography contrast agents. Data from Deslattes et al.[260]

Element	K-edge (keV)
Iodine	33.2
Barium	37.4
Cerium	40.4
Gadolinium	50.2
Ytterbium	61.3
Hafnium	65.4
Tantalum	67.4
Tungsten	69.5
Osmium	73.9
Platinum	78.4
Gold	80.7
Bismuth	90.5